

# Exact Gradients and Hessians for Quantum Optimal Control and Applications in Many-Body Matrix Product States

Jesper Hasseriis Mohr Jensen<sup>1</sup>, Frederik Skovbo Møller<sup>2</sup>, Jens Jakob Sørensen<sup>1</sup>, and Jacob Friis Sherson<sup>1\*</sup>

<sup>1</sup> *Department of Physics and Astronomy, Aarhus University,  
Ny Munkegade 120, 8000 Aarhus C, Denmark and*

<sup>2</sup> *Vienna Center for Quantum Science and Technology,  
Atominstitut, TU Wien, Stadionallee 2, 1020 Vienna, Austria*

Along with growing experimental capabilities and system sizes, the demand for precise quantum control extending into high-fidelity regimes places increasing emphasis on the role of optimization methodologies and their performance capacities. We discuss the importance of accurate derivatives for efficiently locally traversing and converging in optimization landscapes. Framed in the context of quantum optimal control, we find that the feasibility of meeting this central requirement critically depends on the choice of propagation scheme by deriving analytically exact control derivatives (gradient and Hessian). Even when exact propagation is sufficiently cheap and thus *a priori* constitutes the most obviously accessible scheme, we find, perhaps surprisingly, that it is always much more efficient to optimize the (appropriately) approximate propagators: in a certain sense, approximations in the dynamics is traded off for significant complexity reductions in the exact derivative calculations. We quantitatively verify these claims for a concrete, minimal problem and find that the best schemes (exact derivatives of second-order Trotterization with a certain problem structure) obtain unit fidelity to machine precision, whereas the results from exact propagator schemes are separated consistently at least by an order of magnitude in computation time (using exact derivatives) and in worst case 10 orders of magnitude in achievable fidelity (using approximate derivatives). Further, these gaps will always increase with system size and complexity. We then discuss a many-body Bose-Hubbard model in a form compliant with the best scheme and a t-DMRG algorithm within the matrix product state ansatz. Applying the established concepts and a few additional computational techniques, we optimize the superfluid-Mott insulator transition to fidelities 0.99-0.9999 and find quantum speed limit estimates at system sizes well beyond the reach of exact diagonalization approaches. Benchmarking against earlier, seminal gradient-free work on similar problems, we show that the simpler optimization objectives employed therein are not sufficient for fulfilling high-fidelity requirements (here equivalent to residual diagonal entropy), and find substantial qualitative differences (bang-bang structures) and associated quantitative performance improvements (orders of magnitude) and transformation times (factor three) depending on the comparative measure. Overall, we attribute the success and high efficiency of our methodology to the exact derivatives, which, as presented, are immediately applicable to all pure state-transfer control problems.

## I. INTRODUCTION

The first decades of this millennium has seen rapid experimental and theoretical advances in the preparation and engineering of quantum mechanical systems, heralding the second quantum revolution [1]. With these advances, precise manipulation of fragile quantum systems becomes increasingly important. For example, quantum information and computation necessitates control protocols to implement a desired unitary or quantum state preparation with high-fidelity requirements consistent with fault-tolerance thresholds [2–5]. For pure state transfers between eigenstates, this can also be understood as minimizing the diagonal entropy [6–8] at the end of the process. A second requirement for such transformations is that they must be carried out below the detrimental decoherence time scales, preferably at the quantum speed limit [9–11], while also respecting the constraints of the experimental setup. The framework

of quantum optimal control has been a particularly successful tool both theoretically and experimentally for extracting controls satisfying all of these requirements with wide applications in numerous research areas [12], such as superconducting qubits [13–17], nuclear magnetic resonance systems [18–22], nitrogen vacancy centers [23–26], cold molecules [27–30], and cold atoms [31–36], to name a few. At the same time, an increasing array of algorithmic approaches are available in these arenas, counting among others derivative-based (GRAPE [19, 37, 38], GOAT [39], GROUP [22, 40], Krotov [41–43]), derivative-free (Nelder-Mead CRAB [31, 32, 44], stochastic ascent [45], genetic evolutionary [46]), and combinations thereof [47]. Along a separate axis lies additional choices of open-loop [48, 49], closed-loop [50–52], and/or human-in-the-loop [53, 54] control.

Regardless of particulars pertaining to the physical platforms and angles of attack for the optimization itself, a shared common denominator is inevitable: in tandem with growing problem complexity and numerical simulation efforts, the relative efficiency of each optimization cycle must be maximized to allow convergence to high-fidelity solutions within finite time. Accuracy and com-

---

\* [sherson@phys.au.dk](mailto:sherson@phys.au.dk)

putational speed have been identified as important goals and challenges for modern control design [12], and in the context of gradient-based methods, this has been recognized at least since a seminal work Ref. [19] where the analytical first-order approximation to the gradient was calculated. This first-order approximation, however, is not suited for obtaining standard quasi-Newton search directions due to the rapid error accumulation in the Hessian approximation, which is built iteratively from gradients [55]. The steepest descent direction is also only a minimally viable choice with the weakest convergence properties. The use of quasi-Newton methods with the more desirable convergence properties was enabled later in Ref. [37] where the analytically exact gradient for an exact propagator was calculated at the expense of additional computational time per iteration. As system sizes increase, however, exact propagators become infeasible.

In the first part of this work, we hope to advance the theoretical toolbox for obtaining high-fidelity state transfer controls in a formalistically general setting by deriving *analytically exact* gradients as well as Hessians for different propagation schemes, specifically the exact propagator and two second-order Suzuki-Trotter propagators, which we interpret in terms of optimization landscapes. This means that each choice of effective time evolution operator gives rise to its own (not necessarily exact) optimization landscape. Apart from the (sometimes computationally infeasible) exact approach, we thus examine the interplay between approximations in the landscape versus in the derivative calculations. We note that the exact gradient derivation for the exact propagator is similar to the calculations in Ref. [37], but for pure states and not necessarily linear control Hamiltonians – the remaining five derivatives are, to our knowledge, not yet present in the literature. We show that the complexity of exact analytical derivatives strongly depend on the chosen scheme (corresponding to numerical implementation details) and representation of the problem: solving the problem in a basis where the controllable part of the Hamiltonian is diagonal and simultaneously employing one of the Trotterized propagators greatly simplifies the derivative calculations. Especially, the exact gradient for the exact landscape entails a detrimental infinite recursive commutator summation in powers of the time step where the first term corresponds to a first-order approximation. On the other hand, the infinite series terminates identically for the Trotterized landscapes and only the first-order term is needed to be analytically exact. Thus, with those considerations, *analytically exact* gradients can be computed very efficiently, principally limited only by the time it takes to propagate states. To cement these findings and novel calculations, we optimize a two-level LZ problem and indeed find that optimizing in the Trotterized landscapes rapidly yields optimal results to machine precision for that problem. Optimizing in the exact landscape is also feasible if using exact derivatives, where solutions of the same quality are obtained but is an order of magnitude slower per iteration. Using instead the

first-order approximation to the derivatives consistently yields 10 orders of magnitude worse results, while also being slower per iteration. The demonstration shows that, even in a minimal problem, optimizing in the Trotterized landscapes with appropriate exact derivatives is hugely beneficial. The feasibility gap to the exact landscapes will always increase in the face of more complex and larger systems, and this becomes especially relevant when the system size enters the many-body regime, where exact diagonalization, exact propagation, and infinite summation in the associated derivatives are completely outside numerical feasibility.

The simulatory treatment of many-body systems using exact diagonalization approaches is stifled by unfavorable scaling of the Hilbert space dimensionality, requiring an exponential amount of storage and computation time [56]. This lamented *curse of dimensionality* can be broken, however, by invoking specialized ansätze from the broad framework of tensor networks. Briefly, the exponential scaling is in a sense a “convenient illusion” since the majority of physically relevant states, usually characterized by low-entanglement (notably ground states and reachable states from these in finite time), occupy only a small corner of the full Hilbert space [56]. Tensor networks and their bespoke algorithms are a way to target exactly this much reduced subspace with subexponential resources [16, 57, 58]. The success of such approach is owed to the fact that size of the corner is governed by favorable so-called area scaling laws [59]. In the case of 1D systems, the appropriate class of tensor network is *matrix product states* (also known as tensor trains), which exhibits a constant area scaling law with the number of particles [60].

Quantum optimal control of many-body matrix product states was first illustrated in Ref. [31] and later achieved impressive experimental success in Ref. [32] where the superfluid-Mott insulator transition was driven in an optical lattice by adjusting the ratio of characteristic energies  $U/J$ . Here, the superfluid phase is associated with  $J \gg U$  in which the ground state  $|\text{SF}\rangle$  is a delocalized particle distribution across the lattice and the Mott insulator phase with  $U \gg J$  in which the ground state  $|\text{Mott}\rangle = |1, 1, \dots, 1\rangle$  (assuming unit filling) is a single Fock component. The  $|\text{Mott}\rangle$  state is a candidate for, among others, quantum information processing [61] and quantum simulation of spin systems [62], but entering it from the  $|\text{SF}\rangle$  state is non-trivial as the perfect adiabatic transfer  $|\text{SF}\rangle \rightarrow |\text{Mott}\rangle$  timescales diverge near the critical point of  $U/J$  in the thermodynamic limit [31]. Similar tasks of dynamically connecting ground states on either side of a many-body quantum phase transition in minimal time has been studied in [63], where also the role of the critical (minimal) energy gap along optimal trajectories and perspectives to the paradigmatic LZ model were investigated. More generally it has been shown that matrix product states can be efficiently controlled [58].

In both Refs. [31, 32], gradient-free optimization methodologies of the specialized optimization objectives

(averages over density of defects and site variances) were sufficient for the experimental measurement capabilities under consideration. However, as experimental capabilities advance and new avenues for quantum technologies become feasible, the demand for perfect control of the desired quantum state, as measured by the fidelity, exceeds the achievable precision limits encoded by such more lenient figures of merit. More recently, first-order approximation gradient steepest descent was applied to spin- $\frac{1}{2}$  chain systems in Ref. [64]. To our knowledge, this marks the first derivative-based optimization of matrix product states. However, the same restrictions and complications discussed at length in the first part of the paper are suffered due to inexact gradients, which is also pointed out by the authors of Ref. [64] as a concluding remark.

In the second part of this work, we apply our exact derivative methodologies to a problem in the complex many-body regime using a Trotterized propagator with diagonal controls and demonstrate that they are persistently efficient and viable for fidelity requirements above 0.99. To further this endeavor, we also present a t-DMRG algorithm for the matrix product state ansatz that directly embraces the necessary problem structure and apply homotopy methods enabled by the exactness of the derivatives. Specifically, we consider the homogeneous Bose-Hubbard model and drive the superfluid-Mott insulator transition similarly to Refs. [31, 32] and obtain significant quantitative improvements over these benchmarks. Instead of employing more lenient and situationally specific figures of merit, we find that all the fidelity-optimized controls belong to feature-rich, bi-segmentational solution strategies: the first segment corresponds to a slow, but highly non-adiabatic, crossing of the phase transition that mainly homogenizes the site population, whereas the second segment is a bang-bang-type structure that alternates between tunneling events and population locking where a suitable  $c$ -phase is imprinted on individual state components. We find that the optimal number of bangs depend on the transfer duration. This is in the stark qualitative contrast to the very smooth, bang-free benchmark controls, and serves to illustrate that high-fidelity requirements can in some situations necessitate more complex physical processes and elaborate mechanisms, i.e. an increased information-theoretic *control complexity* [8, 58].

## II. EXACT DERIVATIVES FOR QUANTUM OPTIMAL CONTROL

In quantum optimal control we seek to steer some quantum mechanical process in a controlled way such as to maximize a desired physical yield. The manipulatory access to the system dynamics is through one or more control parameters in the Hamiltonian,  $\hat{H} = \hat{H}(u(t))$ . A broad class of control problems deal with maximizing a state transfer  $|\psi_{\text{ini}}\rangle \rightarrow |\psi_{\text{tgt}}\rangle$ , ideally to near unit fidelity

or equivalently zero cost, given respectively by

$$F = |\langle \psi_{\text{tgt}} | \psi(T) \rangle|^2 = |\langle \psi_{\text{tgt}} | \hat{\mathcal{U}}(T; 0) | \psi_{\text{ini}} \rangle|^2, \quad (1)$$

$$J_F = \frac{1}{2} (1 - F), \quad (2)$$

where  $|\psi_{\text{tgt}}\rangle$  is the target state,  $|\psi_{\text{ini}}\rangle$  is the initial state,  $|\psi(T)\rangle = \hat{\mathcal{U}}(T; 0) |\psi_{\text{ini}}\rangle$  is the time evolved state at final time  $T$  with  $\hat{\mathcal{U}}(T; 0)$  being the time evolution operator from  $t = 0 \rightarrow T$ . For numerical convenience it is natural to discretize time in regular  $\delta t$  intervals, leading to piecewise constant time evolution operators

$$t \in [t_1, t_2, \dots, t_{N_t}] = [0, \delta t, \dots, T], \quad (3)$$

$$\hat{\mathcal{U}}(T; 0) = \prod_{j=1}^{N_t-1} \hat{\mathcal{U}}_j = \hat{\mathcal{U}}_{N_t-1} \dots \hat{\mathcal{U}}_2 \hat{\mathcal{U}}_1 \quad (4)$$

where each  $\hat{\mathcal{U}}_n = \hat{\mathcal{U}}(u_n) = \exp(-i\hat{H}(u_n)\delta t)$  with  $u_n = u(t_n)$  evolves the state as  $|\psi_{n+1}\rangle = \hat{\mathcal{U}}_n |\psi_n\rangle$  and  $|\psi_1\rangle = |\psi_{\text{ini}}\rangle$ . For complete generality, assume  $\hat{H}(u_n) = \hat{H}_n^d + \hat{H}_n^c$  where  $\hat{H}_n^c = H(t_n, u_n)$  and  $\hat{H}_n^d(t_n)$  are the control and drift Hamiltonians, respectively.

The task thus consists in finding appropriate control vector(s)  $\vec{u} = (u_1, \dots, u_{N_t})^T$  that minimizes (2) corresponding to local (hopefully global) minima in the control landscape defined by  $J_F = J_F(\vec{u})$ . There are a plethora of techniques and ideas to maneuver the landscape in search of such minima. In this paper we focus on derivative-based local optimization methodologies, characterized by making informed decisions in traversing the control landscape  $\vec{u}^{(k)} \rightarrow \vec{u}^{(k+1)}$  using local information about the landscape topography. Concretely, in prototypical linesearch-based updates on the form

$$\vec{u}^{(k+1)} = \vec{u}^{(k)} + \alpha^{(k)} \vec{p}^{(k)}, \quad \alpha^{(k)} \in \mathbb{R}^+, \quad (5)$$

the search direction  $\vec{p}^{(k)}$  is calculated from the current local gradient (e.g. steepest descent, conjugate gradient, quasi-Newton directions) and possibly also the Hessian (e.g. Newton direction), whereas the step size  $\alpha^{(k)}$  is determined by an inexact linesearch [55].

Accurate control derivatives are paramount in successfully traversing the optimization landscape, since inaccuracies (or willful approximations) yield poor search directions and may significantly slow down, altogether prevent convergence, and limit the achievable fidelity. This is particularly true for quasi-Newton methods, where successive gradients are utilized to approximate the Newton direction; gradient inaccuracies will accumulate with each iteration and completely scramble the Hessian approximation as the optimization progresses (referred to as the “slowdown” problem in Ref. [37]). Additionally, the exact Newton direction itself is typically several orders of magnitude more expensive to construct, and inaccuracies in either derivative is sure to negate any of the potential gains from the extra computational effort, discouraging its use. Finally, the

steepest descent direction is always an unattractive option, since it is well-known to have the worst general properties and convergence rate even when the exact gradient is used (linear as opposed to super-linear and quadratic for quasi-Newton and Newton directions, respectively), and any gradient inaccuracies will enhance this effect. These considerations are generic and not limited to the field of quantum control. In the following we calculate the exact derivatives for pure state transfers to surpass all these issues and verify the claims and calculations by demonstration.

### A. Optimization Landscapes and Exact Derivatives

Complete specification of a control problem includes the time-evolution operator implementation as shown in the following. We will refer to the *exact* and second-order *Suzuki-Trotter* (or *Trotterized*) propagators, respectively, as

$$\hat{\mathcal{U}}_n^{\text{Ex}} = \hat{\mathcal{U}}_n, \quad (6)$$

$$\hat{\mathcal{U}}_n^{\text{ST}_1} = \hat{\mathcal{U}}_{n+1}^{c/2} \hat{\mathcal{U}}_n^d \hat{\mathcal{U}}_n^{c/2} = \hat{\mathcal{U}}_n^{\text{Ex}} + \mathcal{O}(\delta t^3), \quad (7)$$

$$\hat{\mathcal{U}}_n^{\text{ST}_2} = \hat{\mathcal{U}}_n^{c/2} \hat{\mathcal{U}}_n^d \hat{\mathcal{U}}_n^{c/2} = \hat{\mathcal{U}}_n^{\text{Ex}} + \mathcal{O}(\delta t^3), \quad (8)$$

with the definitions

$$\hat{\mathcal{U}}_n \equiv e^{-i\hat{H}_n \delta t}, \quad \hat{\mathcal{U}}_n^{c/2} \equiv e^{-i\hat{H}_n^c \delta t/2}, \quad \hat{\mathcal{U}}_n^d \equiv e^{-i\hat{H}_n^d \delta t}, \quad (9)$$

in units where  $\hbar = 1$  (as expanded on in Sec. III). Note that the operator splitting  $\hat{\mathcal{U}}_n^{\text{ST}_1}$  entails the control points both at  $n$  and  $n+1$  [65], whereas the  $\hat{\mathcal{U}}_n^{\text{ST}_2}$  splitting scheme is fully local in  $n$  with the same error [66]. Although either of these choices are valid to approximate the dynamics and appears on the same footing, their derivative calculations and final expressions are different, underscoring that the precise specification of the implementation is central for use in optimal control contexts (the approximations in derivatives should “match” those of the dynamics).

Numerically, the exact propagator corresponds to direct exponentiation of the Hamiltonian matrix, an operation that scales extremely poorly for increasing Hilbert space dimension  $D_{\mathcal{H}}$ . The Trotterized propagators, on the other hand, lend themselves more readily to a variety of very efficient, problem dependent implementations through e.g. the use of sparsity structures and has a much more benign Hilbert space scaling, extending its applicability far beyond the exact propagator approach.

The local  $\mathcal{O}(\delta t^3)$  Trotterization errors accumulate throughout the evolution defined by Eq. (4), yielding an overall error  $\mathcal{O}(\delta t^2)$ . It is convenient to interpret this as an error with respect to the (“true”) exact landscape,

$$J_F^{\text{ST}}(\vec{u}) = J_F^{\text{Ex}}(\vec{u}) + \mathcal{O}_{J_F^{\text{ST}}}(\delta t^2), \quad (10)$$

for  $\text{ST} = \text{ST}_1, \text{ST}_2$ . The granularity of  $\delta t$  determines how faithful the representation is and, in particular, it follows

that geometric entities for the *same*  $\vec{u}$  are generally different in the three landscapes, e.g. the landscape height (cost value), derivatives, and thus also the search directions for optimization. Importantly, the optimal controls associated with optima in the Trotterized landscapes at large finite  $\delta t$  may not correspond to optima in the exact landscape, which is equivalent to the target not being obtained when propagating said controls using Eq. (6). As  $\delta t \rightarrow 0$ , however, the Trotterized landscapes continuously deform into the exact landscape, and below some sufficiently small finite  $\delta t$  they represent it with only slight modifications. As the landscapes transitively inherit the numerical implementation properties of their associated propagator, there is ample impetus for studying these proxy landscapes.

Detailed calculations of the analytically exact derivatives are given in Appendix A. The results for the gradients are

$$\frac{\partial J_F^{\text{Ex}}}{\partial u_n} = \Re \left( i o^* \left\langle \chi_n \left| \hat{H}_n^{c'} \right| \psi_n \right\rangle \right) \delta t + \mathcal{O}_{\nabla J_F^{\text{Ex}}}(\delta t^2), \quad (11)$$

$$\frac{\partial J_F^{\text{ST}_1}}{\partial u_n} = \Re \left( i o^* \left\langle \chi_n \left| H_n^{c'} \right| \psi_n \right\rangle \right) \delta t, \quad (12)$$

$$\frac{\partial J_F^{\text{ST}_2}}{\partial u_n} = \Re \left( \frac{i o^*}{2} \sum_{p=n}^{n+1} \left\langle \chi_p \left| \hat{H}_n^{c'} \right| \psi_p \right\rangle \right) \delta t, \quad (13)$$

where  $|\chi_n\rangle = \hat{\mathcal{U}}_n^\dagger |\chi_{n+1}\rangle$  is the backwards propagated target state ( $|\chi_{N_t}\rangle = |\psi_{\text{tgt}}\rangle$ ),  $o = \langle \chi_{N_t} | \psi_{N_t} \rangle$  is the transfer amplitude, and  $\hat{H}_n^{c'} = \partial \hat{H}_n^c / \partial u_n$  is the control derivative Hamiltonian. Thus, the gradients for  $J_F^{\text{Ex}}$  and  $J_F^{\text{ST}_1}$  are the same only to first order in  $\delta t$ : whereas  $\nabla J_F^{\text{ST}_1}$  is *analytically exact* with just the  $\delta t$  term,  $\nabla J_F^{\text{Ex}}$  entails an expensive remainder term beyond the first-order approximation. Note on the contrary that  $\nabla J_F^{\text{Ex}}$  and  $\nabla J_F^{\text{ST}_2}$  do *not* coincide even to first order.

Defining the recursive commutator as

$$[X, Y]_k = [X, [X, Y]_{k-1}], \quad [X, Y]_0 = Y, \quad (14)$$

the remainder term entails an infinite series,

$$\mathcal{O}_{\nabla J_F^{\text{Ex}}}(\delta t^2) \propto \left\langle \chi_n \left| \left( \sum_{k=1}^{\infty} \frac{i^k \delta t^k}{(k+1)!} [\hat{H}_n, \hat{H}_n^{c'}]_k \right) \right| \psi_n \right\rangle \delta t, \quad (15)$$

where the first-order approximation in Eq. (11) is the  $k=0$  term. In numerical application, the summation continues until machine precision or some lower desired accuracy, corresponding to some  $k_{\text{max}}$ . This is necessary because, generally, the Hamiltonian and its control derivative do not commute  $[\hat{H}_n, \hat{H}_n^{c'}] \neq 0$  and the recursive commutator is not guaranteed to terminate and may even grow (as measured by some appropriate norm) with  $k$ . A few examples include  $\hat{H} = \sigma_x + u(t) \cdot \sigma_z$  where  $\sigma_i$  are spin operators,  $\hat{H} = \hat{T} + \hat{V}(u(t))$  where  $\hat{V}$  ( $\hat{T}$ ) is the potential (kinetic) energy operator for a single particle, or the Bose-Hubbard Hamiltonian later defined in



Eq. (18). Note that, as we shall see below, the presence of the infinite sum means that in the context of optimization, perhaps surprisingly, it may not be desirable to use exact time evolution even if it is readily available.

For the Trotterized landscapes, the calculation of  $\nabla J_F^{\text{ST}_1}$  and  $\nabla J_F^{\text{ST}_2}$  contains an infinite series of the same structure, but with  $\hat{H}_n \rightarrow \hat{H}_n^c$  in the first argument of the recursive commutator. A central additional (mild) assumption is that the control Hamiltonian is given in its diagonal representation, in which case  $[\hat{H}_n^c, \hat{H}_n^{c'}]_k = \hat{H}_n^{c'} \cdot \delta_{0,k}$  because two diagonal matrices always commute, and the series terminate after  $k_{\text{max}} = 0$  exactly. Incidentally, in many cases the “natural” basis states for computations are already the ones that diagonalize  $\hat{H}_n^c$ , e.g. spin eigenstates ( $|\uparrow\rangle, |\downarrow\rangle$ ), position eigenstates ( $|\vec{x}\rangle$ ), or site-occupation eigenstates ( $|n_i\rangle$ ) for the Hamiltonians mentioned above. The operator splitting and control diagonality has additional computational benefits because it disentangles and trivializes the control and drift exponential calculations:  $\hat{U}_n^{c/2}$  is cheap to calculate (diagonal matrix exponentiation is the element-wise exponentiation of the diagonal), and the possibly expensive calculations of  $\hat{U}_n^d$  for all  $n$  can be performed once and stored in memory or on the disk (it is by definition independent of the choice of  $\vec{u}$ ). This allows performance boosts at runtime.

### B. Demonstration: Optimizing in Exact and Trotterized Landscapes

To quantitatively verify the assertions made in this section on a concrete problem, we consider the canonical LZ model with  $\hat{H}_n = \hat{H}^d + \hat{H}_n^c = \frac{1}{2}(\sigma_x + u_n \cdot \sigma_z)$  and the state transfer  $|\psi_{\text{ini}}\rangle = |\uparrow\rangle \rightarrow |\psi_{\text{tgt}}\rangle = |\downarrow\rangle$ . The reason for choosing this problem in particular is twofold. First, it has well-understood solutions [67] with a single, analytical time-optimal solution  $u_n = 0$  at  $T_{\text{opt}} = \pi$  and remains solvable beyond this duration. Second, despite its simplicity, the model remains prototypical even in the context of many-body arena. For example, many-body dynamics can in certain scenarios be thought of as a cascade of independent LZ transitions and similar characteristics between LZ and some many-body control problems have been found [11, 63, 68].

Figure 1 shows the optimization results. From the  $1-F$  iteration trajectories we find that unit fidelities (to machine precision) are easily obtainable when utilizing any of the exact gradients, with some variance in the number of iterations needed. When a solution approaches the optimum, very rapid convergence is observed. Looking, however, at the optimization wall time trajectories provides some nuance since two very well-defined bands obtaining unit fidelity appears. The band constituted by the green and orange trajectories is separated by an order of magnitude in computation time from the band constituted by the blue trajectories. These bands are associated with the Trotterized and exact landscapes, respectively, and the separation is due to both the  $k_{\text{max}} = 15$

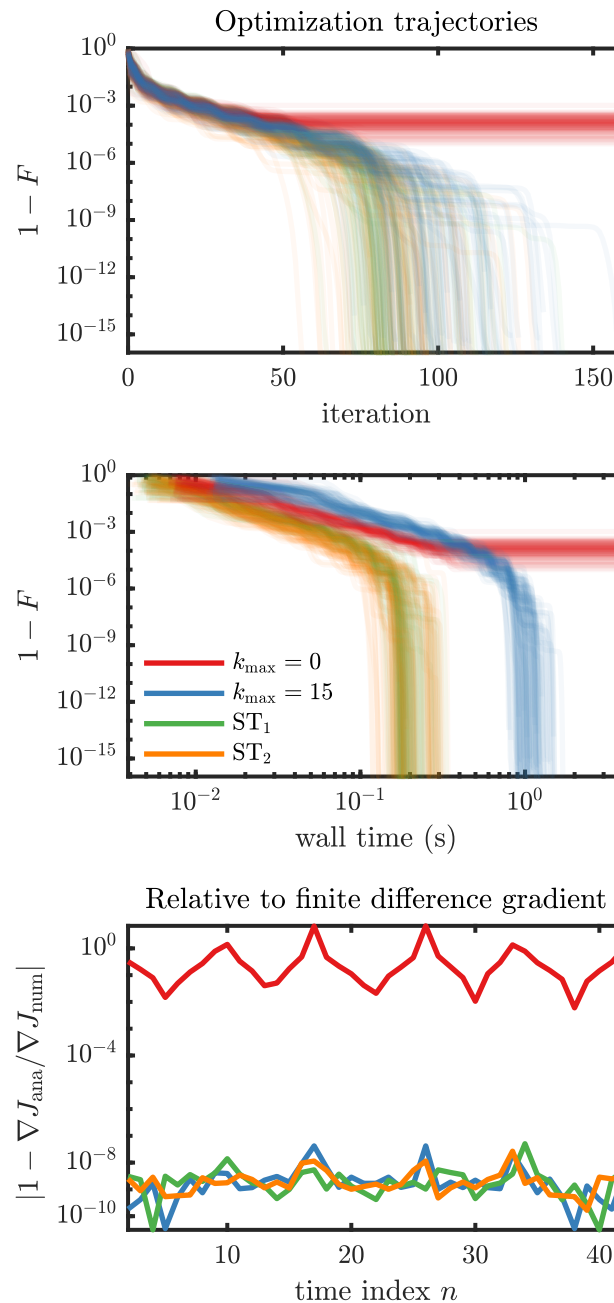


FIG. 1. Demonstration of optimizing in exact- and Trotterized landscapes for the simple two-level LZ problem. Top and middle: At  $T = 1.01\pi \gtrsim T_{\text{opt}}$  with  $\delta t = 0.075$  and for the same uniformly randomly generated seeds,  $u_n = \text{uniform}(-20, 20)$ , we optimize with the BFGS search direction (as implemented in MATLAB’s `fminunc`) in four different scenarios: exact propagator with first-order ( $k_{\text{max}} = 0$ ) and exact ( $k_{\text{max}} = 15$ ) gradients, and both Trotterized propagators with exact gradients. Out of 100 seeds, only 11 (not shown) did not converge to machine precision in 400 iterations when using exact gradients. Bottom: Analytical gradients ( $\nabla J_{\text{ana}}$ ) relative to their numerical central finite difference approximation ( $\nabla J_{\text{num}}$ ) with perturbation  $\epsilon = \epsilon_{\text{mach}}^{1/3}$  for a constant example control with  $u_n = 5$ .

tail in Eq. (15) and the difference in propagation computation time.

As opposed to the exact gradients, the first-order gradient approximation  $k_{\max} = 0$  in the exact landscape performs significantly worse. It prevents convergence to unit fidelities by more than 10 orders of magnitude while also being slower compared to iterations in the Trotterized landscapes. Comparing the analytical gradients to numerical finite difference gradients further shows that the first-order approximation can be very poor, whereas the exact ones are in close agreement. Note that the central finite difference gradients themselves are associated with errors of order  $\mathcal{O}_{\nabla J_F}(\delta t^2)$ .

For simplicity we chose a static truncation parameter such that  $\delta t^{k_{\max}} \lesssim \epsilon_{\text{mach}}$  where  $\epsilon_{\text{mach}} = 2.22 \cdot 10^{-16}$  is the machine precision for the double-precision floating-point format. With decreasing  $\delta t$ , the necessary  $k_{\max}$  for exact gradients also decreases and the  $k = 0$  term becomes increasingly dominant. Indeed, running the same optimizations as in Fig. 1 for  $\delta t = 0.025$ , the  $k_{\max} = 0$  optimization yields 2-3 orders of magnitude better final results, and at  $\delta t = 0.01$  the first-order approximation is sufficient for finding machine precision unit fidelities. That is, reducing the number of  $k$  terms required for accurate gradients is traded off for increased computation time per iteration due to additional time evolutions. As a consequence of the much larger computational overheads in computing the exact matrix exponential, the  $k_{\max} = 0$  trajectories remains similarly separated from the Trotterized trajectories even though it may now be sufficient in terms of final results. We also tried the smallest  $k_{\max} = 9$  such that  $\delta t^{k_{\max}} / (k_{\max} + 1)! \lesssim \epsilon_{\text{mach}}$  and a dynamic scheme (since the recursive commutator depends on  $u_n$ ) based on the infinity norm of subsequent terms being smaller than  $\epsilon_{\text{mach}}$  and found virtually no difference to the presented results, but we expect that the dynamic scheme in particular may be more appropriate outside of this minimal problem. It is also likely that a less conservative  $\epsilon < \epsilon_{\text{mach}}$  threshold may be used. In any event, the question of the best strategy for choosing the smallest  $k_{\max}$  that produces sufficiently exact gradients depends intimately on the problem at hand and its parameters, and there may not be a definite answer. The exact Trotter derivatives are on the other hand irrespective of  $\delta t$  in terms of complexity. This allows among others effective use of *homotopy* methods as discussed later in Sec. IV.

The gradient  $\nabla J_F^{\text{ST}_2}$  is slightly more involved to implement than  $\nabla J_F^{\text{ST}_1}$  due to the factor 2 increase in the number of overlap calculations, although this is marginal compared to the time evolution computational effort. We nevertheless take  $\hat{\mathcal{U}}_n^{\text{ST}_1}$  to be our propagator of choice in the remainder of the paper and note that similar calculations and arguments apply to the analytically exact Hessians, but in this case, the expressions for  $\nabla^2 J_F^{\text{Ex}}$  and  $\nabla^2 J_F^{\text{ST}_2}$  are much more complicated than  $\nabla^2 J_F^{\text{ST}_1}$  as shown in Appendix A.

In conclusion, the immediate advantages of optimiz-

|                                 | Applicability | Landscape error           | Derivative error            |
|---------------------------------|---------------|---------------------------|-----------------------------|
| $\hat{\mathcal{U}}^{\text{Ex}}$ | Small systems | Exact                     | $\mathcal{O}(\delta t^2)^*$ |
| $\hat{\mathcal{U}}^{\text{ST}}$ | Any           | $\mathcal{O}(\delta t^2)$ | Exact                       |

TABLE I. The exact- and Trotterized propagator properties where ST = ST<sub>1</sub>, ST<sub>2</sub> and the ‘\*’ assumes the first-order approximation (truncation to  $k_{\max} = 0$  in Eq. (11)). The exact propagator is feasible only for small systems due to the direct operator exponentiation. The derivatives in the Trotterized landscapes are exactly calculable under diagonal assumptions while simultaneously having a greatly reduced computational cost regardless of system size and value of  $\delta t$ . Exact derivatives are very important for convergence.

ing in the Trotterized landscapes over the exact landscape are twofold: i) they are applicable to much larger systems, and ii) their analytically exact control derivatives and thus search directions (essential for optimization convergence) are greatly simplified under an assumption that can always be (and often is automatically) fulfilled. The only implicit requirement is that  $\delta t$  is small enough for the Trotterization to faithfully approximate the exact dynamics, or equivalently the exact landscape Eq. (10). The exact propagator can, nonetheless, still be used if the Hilbert space is sufficiently low-dimensional such that the direct exponentiation and series summation becomes feasible. However, even for the simplest possible non-trivial problem in Fig. 1 this approach is seen to be much slower than the alternative. These main conclusions are summarized in Table I.

Lastly, we would like to point out that the results in this section followed a discretize-then-optimize (discretization before ordinary vector derivatives of a cost function) rather than optimize-then-discretize (discretization after continuous Gâteaux derivatives of a cost functional) approach. Since these approaches do not in general necessarily yield the same derivative expressions, the former approach is preferable because it specifically takes into account the chosen propagation scheme implementation (the derivatives “match” the landscape/dynamics) which has been a main point throughout this section. It is therefore quite a happy coincidence that e.g. i) the exact propagator gradient  $\nabla J_F^{\text{Ex}}$  calculated by the optimize-then-discretize approach yields exactly the same expression as  $\nabla J_F^{\text{ST}_1}$ , and ii)  $\hat{\mathcal{U}}^{\text{ST}_1}$  is a standard propagator for many systems, e.g. for wave functions in real space. The combined effect is that the sought after exactness of the derivatives are obtained by virtue of standard methods alone in these situations, knowingly or otherwise. Note that the same would not be true if  $\hat{\mathcal{U}}^{\text{Ex}}$  or  $\hat{\mathcal{U}}^{\text{ST}_2}$  was used.

### III. PHYSICAL MODELING

In this section, we recount the fundamentals of the Bose-Hubbard model [69–71] and recast it in the form required for simplified calculations of the exact derivatives introduced in Sec. II. We then briefly present the many-body ansatz of matrix product states – for an excellent, detailed introduction see Ref. [66]. Finally, we discuss a t-DMRG algorithm tailored to the necessary problem representation to significantly accelerate computations.

#### A. Bose-Hubbard State Transfer

The physical description of  $N_p$  spinless interacting bosons for a quasi-1D periodic potential of  $N_s$  sites in absence of additional external fields is captured by the Bose-Hubbard Hamiltonian in SI units

$$\hat{H}_{\text{SI}} = \hat{H}^J + \hat{H}^U = J_x \sum_{i=1}^{N_s-1} \hat{h}_{[i,i+1]}^{J_x} + \frac{U}{2} \sum_{i=1}^{N_s} \hat{h}_{[i]}^U, \quad (16)$$

$$\hat{h}_{[i,i+1]}^{J_x} = -(\hat{a}_{i+1}^\dagger \hat{a}_i + \text{h.c.}), \quad \hat{h}_{[i]}^U = \hat{n}_i(\hat{n}_i - 1) \quad (17)$$

where  $J_x$  is the (site-isotropic) strength associated with the hopping (tunneling) operator  $\hat{h}_{[i,i+1]}^{J_x}$  along the  $x$  direction, and  $U$  is the energy associated with the on-site interaction operator  $\hat{h}_{[i]}^U$ . Here,  $\hat{a}_i^\dagger$  ( $\hat{a}_i$ ) is the creation (annihilation) operator associated with the lowest band Wannier function (maximally localized) on site  $i$ . The ratio  $U/J$  characterizes the phases of the system: we associate with  $J \gg U$  the superfluid phase in which the ground state  $|\text{SF}\rangle$  is a delocalized particles distribution across the lattice with sizeable site occupation variance and with  $U \gg J$  the Mott insulator phase in which the ground state  $|\text{Mott}\rangle = |1, 1, \dots, 1\rangle$  (assuming  $N_p = N_s$ ) is a single Fock component.

We consider a realization of the model in a cubic optical lattice loaded with ultra cold atoms. The characteristic energies  $J_x(v_x)$  and  $U(v_x, v_y, v_z)$  are then implicitly related to the trapping depths  $v_x, v_y, v_z$  as denoted, see Appendix B.

For the phase transition [72–74] transfer  $|\text{SF}\rangle \rightarrow |\text{Mott}\rangle$  in an experimental realization, the tunable parameters at hand in this instance are the lattice depths, and at first glance, the natural choice for a control is  $u = v_x$ . It is more fruitful, however, to non-dimensionalize Eq. (16) by  $\hat{H} = \hat{H}_{\text{SI}}/J_x$  to obtain control, drift, and control derivative Hamiltonians (defined in Sec. II)

$$\hat{H}_n = \hat{H}^d + \hat{H}_n^c = \sum_{i=1}^{N_s-1} \hat{h}_{[i,i+1]}^{J_x} + \frac{u_n}{2} \sum_{i=1}^{N_s} \hat{h}_{[i]}^U, \quad (18)$$

$$\hat{H}^{c'} = \frac{1}{2} \left( \sum_{i=1}^{N_s} \hat{n}_i(\hat{n}_i - 1) \right), \quad (19)$$

where the control parameter is instead  $u_n = U(t_n)/J_x(t_n)$ . The first benefit of this choice is that  $\hat{H}_n^c$

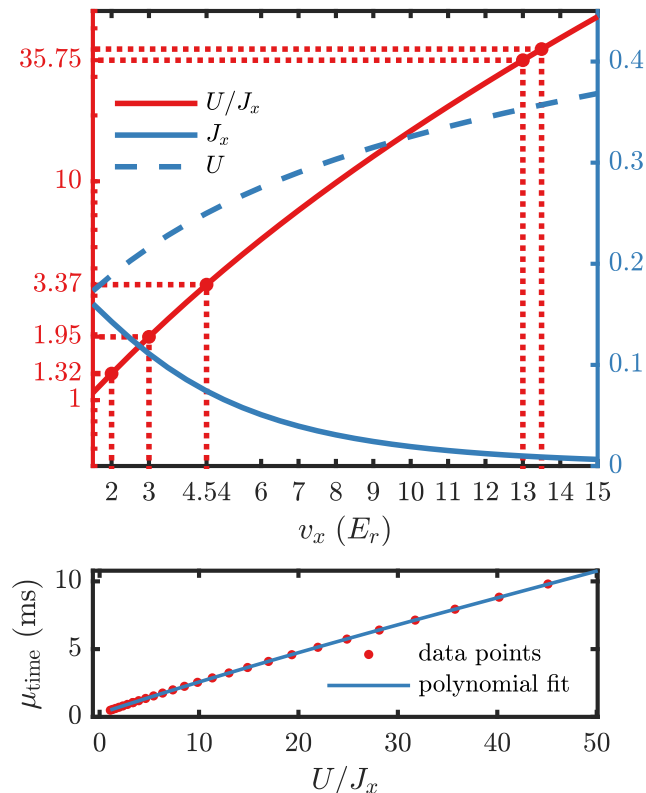


FIG. 2. Constitutive relations  $U(v_x)$ ,  $J_x(v_x)$  (top) and time scaling (bottom) for the concrete system described in the text. The dots denoted on the  $U/J_x$  curve indicate values of note. Left to right, they are: the minimally allowed  $v_x = 2 E_R$ , the  $v_x$  defining  $|\text{SF}\rangle$ , the critical point of the  $|\text{SF}\rangle \rightarrow |\text{Mott}\rangle$  phase transition, the  $v_x$  defining  $|\text{Mott}\rangle$ , and the maximally allowed  $v_x = 13.5 E_R$  (corresponding to  $U/J = 40.18$ ). The time scaling is  $\mu_{\text{time}} = \hbar/J_x(v_x)$  and the transfer duration in SI units Eq. (21) thus depends on the control vector  $\vec{u} = (\dots, (U/J_x)_n, \dots)$ .

is now diagonal (a key assumption for obtaining analytically exact derivatives) when described in the site occupation Fock basis. The second is that both the control derivative and drift Hamiltonian are time-independent, and the latter can be exploited to accelerate computations as shown later in this section. The third is that the optimal controls are system agnostic, i.e. irrespective of the physical platform. Thus, constitutive equations such as Eqs. B3-B4 must be used to map the optimized  $U/J_x$  ramp into the parameters relevant to the specific realization, in this case the trapping depth  $v_x$ . This is likewise reflected following the non-dimensionalization of propagators, and the time-scales become dependent on the control corresponding to lattice depth. Omitting time-

dependence for clarity, we have e.g.

$$\begin{aligned}\hat{\mathcal{U}}^{\text{Ex}} &= \exp\left(-i\frac{\hat{H}_{\text{SI}}\delta t_{\text{SI}}}{\hbar}\right) = \exp\left(-i\frac{\hat{H}_{\text{SI}}}{J_x}\left\{\frac{J_x\mu_{\text{time}}}{\hbar}\right\}\delta t_{\text{sim}}\right) \\ &\stackrel{!}{=} \exp\left(-i\hat{H}\delta t_{\text{sim}}\right) \Rightarrow \mu_{\text{time}} = \hbar/J_x,\end{aligned}\quad (20)$$

and similar for  $\hat{\mathcal{U}}^{\text{ST}}$ . These are working equations corresponding to  $\hbar = 1$  and where  $\delta t_{\text{SI}} = \mu_{\text{time}} \cdot \delta t_{\text{sim}}$ : time steps expressed in SI units,  $\delta t_{\text{SI}}$ , are related to (constant) dimensionless simulation numbers  $\delta t_{\text{sim}}$ , through the time scale  $\mu_{\text{time}} = \hbar/J_x(u_n)$  which depends on the control value. In particular, the total duration of the transfer process given in SI time is

$$T_{\text{SI}}(\vec{u}) = \hbar\delta t_{\text{sim}} \sum_{n=1}^{N_t} J_x^{-1}(u_n), \quad (21)$$

i.e. the relevant time-scales are given by the specific realization of the physical platform and depends on the control vector.

Elsewhere in the paper, subscripts are dropped and we write  $\delta t = \delta t_{\text{sim}}$  and all quantities of time are implicitly given in non-dimensional simulation values unless followed by a unit.

To enable a degree of quantitative comparison, we consider the experimental parameters given in Ref. [32], although we have no additional harmonic trapping. The lattice recoil energy is  $E_R = \hbar^2\pi^2/(2a_s m) \approx 2.03 \text{ kHz} \cdot \hbar$  where  $m = 87 \text{ amu}$  is the mass, and  $a_s = 101a_0$  the  $s$ -wave scattering length of Rubidium 87. Additionally,  $\hbar$  is the Planck constant,  $\hbar$  the reduced Planck constant, and  $a_0$  is the Bohr radius. We assume a lattice of wavelength  $\lambda = 1064 \text{ nm}$  with lattice spacing  $a_{\text{lat}} = \lambda/2 = 532 \text{ nm}$  and fixed transverse trapping depths  $v_y = v_z = 20 E_R$ , and drive the  $|\text{SF}\rangle \rightarrow |\text{Mott}\rangle$  transition defined by

$$|\psi_{\text{ini}}\rangle = |\text{SF}\rangle \equiv |\text{GS}; v_x = 3E_R\rangle \quad (22)$$

$$|\psi_{\text{tgt}}\rangle = |\text{Mott}\rangle \equiv |\text{GS}; v_x = 13E_R\rangle \quad (23)$$

where GS refers to the ground state at the specified longitudinal depth  $v_x$ . The transition is driven by varying the  $v_x$ , with the requirement that  $2E_R \leq v_x$  at all times to satisfy the modeling assumptions in Appendix B. With this choice of parameters, the constitutive equations between  $v_x$  and the energies  $U$  and  $J_x$  are calculated numerically and shown in Fig. 2. The conversion to  $U/J_x$  for several relevant depths  $v_x$  are shown, e.g. at  $(v_x)_{\text{crit}} \approx 4.5 E_R$  that in Ref. [32] corresponds to the critical point for the phase transition. At this depth we obtain  $(U/J_x)_{\text{crit}} \approx 3.4$  which agrees with the number stated in Ref. [32], and we consider this a verification for our numerical calculation of  $J_x(v_x)$  and  $U(v_x, v_y, v_z)$ . As discussed above, the SI time scaling in Eq. (21) depends on  $J_x^{-1}$ . As shown in the bottom of Fig. 2, larger  $U/J_x$  values correspond to larger SI times. Since we desire the fastest possible optimal controls in real time, we

also place an upper bound  $v_x \leq 13.5 E_R$  during optimization to limit this artifact of the non-dimensionalization. With the same reasoning, we add slight preference towards lower control values by introducing a regularization cost term for the control amplitude. Due to limited bandwidth of experimental electronics we also add a regularization cost term for the temporal derivative of the control, slightly shifting preference towards smoother controls. The derivatives for these cost terms are calculated in Appendix A and must be included in the optimization.

## B. Matrix Product States

The general form of a matrix product state for a finite unclosed chain of  $N_s$  constituents (sites) is

$$|\psi\rangle = \sum_{j_1, j_2, \dots, j_{N_s}} \mathbf{A}^{j_1} \mathbf{A}^{j_2} \dots \mathbf{A}^{j_{N_s}} |j_1, \dots, j_{N_s}\rangle, \quad (24)$$

where  $j_i \in \{1, 2, \dots, d\}$  is the *physical index* (degree of freedom) for the  $i$ 'th constituent,  $d$  is the size of the local Fock space, and  $\mathbf{A}^{j_i} \in \mathbb{C}^{a_{i-1} \times a_i}$  where  $a_i$  is the *bond index* with the only requirement that the product of all the matrices yields a scalar. The ansatz Eq. (24) is simply a decomposition of the expansion coefficient  $c_{j_1, j_2, \dots, j_{N_s}}$  tensor of rank  $N_s$  into  $N_s$  rank 3 tensors  $\{A_{a_{i-1}, a_i}^{j_i}\}_{i=1}^{N_s}$ , which is always possible by repeated singular value decomposition (SVD) or similar and is in fact a principally *exact* representation. Properties of e.g. the SVD procedure, however, allows significant truncation of the matrix  $\mathbf{A}^{j_i}$  dimensions (associated with the bond indices) for low-entanglement states: singular values of the SVD corresponds to the expansion coefficients in the Schmidt decomposition across a given bi-partitioning of the system, many of which are close to (or exactly) zero for such states. Thus, we can choose to keep only singular values larger than a given threshold  $s_{\text{max}}$  and/or impose a maximum number values  $D$  to keep, depending on the desired accuracy. Even though the matrix product state is in practice not constructed directly from the coefficients (the storage of which is exponential), virtually all basic matrix product state algorithms, such as diagonalization (DMRG) and time evolution (t-DMRG), similarly employ SVD (or QR) decompositions. This enables a natural way of keeping resource consumption in check, typically by specifying a given  $s_{\text{max}}$  and/or  $D$  in advance.

In the present case of the Bose-Hubbard model Eq. (18) with unit filling,  $j_i$  is the site occupation number and  $d = N_p = N_s$ . The Hilbert space dimension scales exponentially

$$D_{\mathcal{H}} = \frac{(N_s + N_p - 1)!}{N_p!(N_s - 1)!}, \quad (25)$$

which limits the feasibility of exact diagonalization approaches roughly to  $N_p = 10 - 13$  with increasing layers



of analytical and numerical sophistication needed for relatively small gains [75]. At such a low number of sites, the “bulk” of the system is constituted by only a relatively small fraction of sites. Matrix product states, on the other hand, are as mentioned associated with polynomial scaling [56, 57, 66] and can comfortably extend this range into the low-to-mid tens of particles in a time-dependent setting [31, 32, 76] or low hundreds in a static setting [77].

### C. t-DMRG for Bose-Hubbard Model

Time evolution is the fundamental operation for quantum optimal control. For this reason, we present here a t-DMRG variant similar to Ref. [78] tailored to the structure of Eq. (18) to speed up our computations at the cost of an increased Trotterization error per time step,  $\mathcal{O}(\delta t^3) \rightarrow \mathcal{O}(\delta t^2)$ .

We start by considering the second-order Suzuki-Trotter expansion  $\hat{U}_n^{\text{ST}_1} = \hat{U}_{n+1}^{c/2} \hat{U}_n^d \hat{U}_n^{c/2}$  (Eq. (7)) with the non-dimensionalized Bose-Hubbard control and drift Hamiltonians (18) evaluated at time index  $n$ . Each term in the diagonal control Hamiltonian commutes and we may write exactly

$$\hat{U}_n^{c/2} = \exp \left( -i \left( \frac{u_n}{2} \sum_{i=1}^{N_s} \hat{h}_{[i]}^U \right) \frac{\delta t}{2} \right) = \prod_i \hat{U}_{n,[i]}^U, \quad (26)$$

where  $\hat{U}_{n,[i]}^U = \exp(-iu_n \hat{h}_{[i]}^U \delta t/4)$ . For the drift Hamiltonian we can apply the same technique as in standard t-DMRG [66, 79] for nearest-neighbor Hamiltonians to obtain a first-order Suzuki-Trotter expansion with associated error  $\mathcal{O}(\delta t^2)$ ,

$$\begin{aligned} \hat{U}^d &= e^{-i(\hat{H}_{\text{even}}^d + \hat{H}_{\text{odd}}^d)\delta t} \approx e^{-i\hat{H}_{\text{even}}^d\delta t} e^{-i\hat{H}_{\text{odd}}^d\delta t} \\ &= \left( \prod_{i \text{ even}}^{N_s-1} \hat{U}_{[i,i+1]}^{J_x} \right) \left( \prod_{i \text{ odd}}^{N_s-1} \hat{U}_{[i,i+1]}^{J_x} \right), \end{aligned} \quad (27)$$

where  $\hat{U}_{[i,i+1]}^{J_x} = \exp(-i\hat{h}_{[i,i+1]}^{J_x}\delta t)$ . The enabling step in this expansion is to group even and odd terms

$$\hat{H}^d = \hat{H}_{\text{even}}^d + \hat{H}_{\text{odd}}^d = \sum_{i \text{ even}}^{N_s-1} \hat{h}_{[i,i+1]}^{J_x} + \sum_{i \text{ odd}}^{N_s-1} \hat{h}_{[i,i+1]}^{J_x}. \quad (28)$$

Although  $[\hat{H}_{\text{even}}^d, \hat{H}_{\text{odd}}^d] \neq 0$  causes the  $\mathcal{O}(\delta t^2)$  error, each term has total internal-commutativity, allowing the subsequent exact product form Eq. (27). Combining the above expressions and moving each individual even (odd)  $\hat{h}_{[i,i+1]}^{J_x}$  to the left (right) until they meet a non-

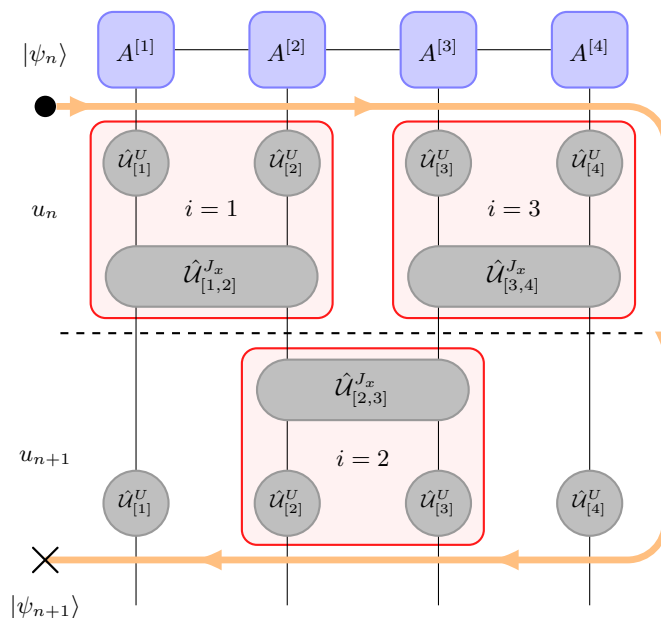


FIG. 3. Example diagram ( $N_s = 4$ ) for t-DMRG tailored to non-dimensionalized Bose-Hubbard Hamiltonian Eq. (18) showing the calculation  $|\psi_{n+1}\rangle = \hat{U}_n^{\text{ST}_1} |\psi_n\rangle$ . The site tensors (blue nodes) are connected bond indices (horizontal lines). The one- and two-site gates (grey nodes, time index suppressed) come in triples (red boxes) and are applied to physical indices of the site tensors (vertical lines), in the order indicated by the thick orange-arrowed line (Eqs. 30-29). The beginning (end) is marked by a black dot (cross), and the dashed line separates the forward sweep with  $u_n$  (above) from the backward sweep with  $u_{n+1}$  (below). Application of product triple  $i$  in the forward sweep entails the following: 1) contract the two site tensors with physical indices  $i, i+1$  over their common bond index into a temporary two-site tensor, 2) apply the two one-site gates followed by the two-site gate, 3) split the temporary two-site tensor by SVD back into two individual site tensors with the central site (gauge) moved to  $i+1$ , and 4) shift the gauge an additional site to the right, such that the central site is at  $i+2$ . Each arrow tip demarcates the gauge position during the sweep, where sites to the right (left) are right(left)-normalized, with the exception that the next site intersecting the orange line is the central site. After applying the first left-over one-site gate, the backward sweep is similarly performed with the following modifications 1) the site indices are  $i-1, i$ , 2) the order of gate application reversed, 3) the central site is placed on  $i-1$ , and 4) the central site is gauged to  $i-2$ . Finally, the second left-over one-site gate is applied, and exactly the same procedure can subsequently be applied to obtain  $|\psi_{n+2}\rangle = \hat{U}_{n+1}^{\text{ST}_1} |\psi_{n+1}\rangle$ . Implementing the backward propagation  $|\psi_n\rangle = \hat{U}_n^{\text{ST}_1\dagger} |\psi_{n+1}\rangle$  is similar, but with reversed arrow tips and order of application.

commutative operator, we obtain for even  $N_s$

$$\hat{\mathcal{U}}_n^{\text{ST}_1} \approx \prod_i^{N_s} \hat{\mathcal{U}}_{n,[i]}^U \prod_{i \text{ even}}^{N_s-1} \hat{\mathcal{U}}_{[i,i+1]}^{J_x} \prod_{i \text{ odd}}^{N_s-1} \hat{\mathcal{U}}_{[i,i+1]}^{J_x} \prod_i^{N_s} \hat{\mathcal{U}}_{n,[i]}^U$$

$$= \hat{\mathcal{U}}_{n+1,[1]}^U \left( \prod_{i=1}^{N_s-1} \hat{\mathcal{U}}_{n+1,[i]}^U \hat{\mathcal{U}}_{n+1,[i+1]}^{J_x} \hat{\mathcal{U}}_{n+1,[i+1]}^U \right) \quad (29)$$

$$\hat{\mathcal{U}}_{n+1,[N_s]}^U \left( \prod_{i=1}^{N_s-1} \hat{\mathcal{U}}_{[i,i+1]}^{J_x} \hat{\mathcal{U}}_{n+1,[i+1]}^U \hat{\mathcal{U}}_{n+1,[i]}^U \right). \quad (30)$$

If  $N_s$  is odd, replace  $\hat{\mathcal{U}}_{n+1,[N_s]}^U \rightarrow \hat{\mathcal{U}}_{n,[N_s]}^U$  in Eq. (30). In the language of matrix product states, application of one-site ( $\hat{\mathcal{U}}_{n,[i]}^U$ ) and two-site gates ( $\hat{\mathcal{U}}_{[i,i+1]}^{J_x}$ ) can be done very efficiently when exploiting left- and right-normalization of the site tensors. The one-site gates are cheap to compute because  $\hat{h}_{[i]}^U$  is diagonal and the two-site gates are time-independent and can be precomputed and stored on the disk, which would otherwise entail the most expensive operation. Additionally, the suggestive grouping of product triples provides a way of reducing overhead in the tensor network contraction  $\hat{\mathcal{U}}_n^{\text{ST}} |\psi\rangle$  by advancing the central site (gauge) of the matrix product state: apply the product of triples and contract the site tensors in a “forward sweep” over odd  $i$  (30) and then in a “backward sweep” over even  $i$  (29) as illustrated and explained in Fig. 3.

#### IV. OPTIMIZATION RESULTS

In this section, we present optimization results using exact derivatives (Sec. II) for the Bose-Hubbard state transfer task (Sec. III A) within the matrix product state ansatz (Sec. III B) employing the accelerated Trotterized propagation scheme (Sec. III C).

We consider a lattice system at unit filling  $N_p = N_s = 20$ . This is comfortably beyond the feasibility of exact diagonalization approaches as the Hilbert space has dimensionality  $D_{\mathcal{H}} \sim 7 \cdot 10^{10}$  and requires  $\sim 550$  GB memory just to store a single state. Our matrix product state computations are performed using the ITENSOR library [80] and we use an auxiliary dimension of  $D = 200$ , a singular value threshold of  $s_{\text{max}} = 10^{-12}$ , and a reduced local Fock space  $d = 5$  (higher local occupation numbers do not contribute significantly to the dynamics due to the exponential on-site energy penalty). We use the DMRG algorithm implemented in ITENSOR to obtain the initial- and target states. For the given system size, the durations required to approach the quantum speed limit for fidelity  $F = 0.99$ ,  $T_{\text{qsl}}^{F=0.99}$ , with sufficiently low landscape (Trotterization) error necessitates about  $N_t = 350 - 450$  time steps for  $\delta t = 0.025$ . To accelerate the optimizations, however, we take  $\delta t$  to be a homotopy (or continuation) parameter: we sequentially optimize on increasingly fine grained time grids, specifically  $\delta t = 0.1 \rightarrow 0.05 \rightarrow 0.025$ . By halving the values, the new grid points coincides with

the old but with doubled resolution (each newly inserted point is set to the value of old point immediately prior corresponding to  $\hat{\mathcal{U}}_n(\delta t) \approx \hat{\mathcal{U}}_n(\delta t/2)\hat{\mathcal{U}}_n(\delta t/2)$ ). The benefit is that the coarser optimizations can yield relatively rapid fidelity improvements since fine grained resolution is typically not needed for the overall shape of the solution. Care should be taken, however, not to spend too long on these, since they are not fully coincidental with the final optimization landscape. Note that this methodology is enabled by the exactness of the Trotterized gradient not being dependent on  $\delta t$ , which is not the case for the exact propagator gradient with finite summation cutoffs (see Eqs. 6-7). For the search direction and step size line searching in Eq. (5), we employ the non-linear interior-point algorithm implemented in IPOPT [81] by supplying the exact derivatives. Briefly, interior-point methods handle control constraints by including them explicitly when solving for the searching direction, which in our case is  $1.32 \leq u_n \leq 40.18$  for all  $n$ . Being a second-order method, the search direction includes the Hessian or a gradient-based approximation thereof (BFGS). We found the exact Hessian calculation (time scale of days per iteration) for the problem under consideration to be outside our time budget even when including the homotopy, and therefore opted for the latter (time scale of hours per iteration) and allowed roughly 3 days of optimization wall time. For the regularizations (Appendix A) we find  $\alpha = 10^{-7}$  and  $\gamma = 10^{-8}$  to be reasonable choices initially. Our seeding strategy is based on an adiabatically inspired reference control overlayed with a sum of random Fourier components. As a verification for our implementation of e.g. the exact analytical derivatives and time evolution, we compared the analytical derivatives to their finite difference counterpart and found that they agreed to at least the same precision as in the LZ problem Fig. 1.

Figure 4 shows the distributions of final infidelities ( $1 - F(T)$ ) before and after optimization for a batch of linearly spaced simulation durations. The corresponding SI durations are not linearly spaced since they depend on the individual control ramps Eq. (21), but there is a close overall resemblance in the shape (a scatter plot of the durations reveals a clear linear relationship with a near-constant variance). The gain in fidelity due to the optimization is significant: all seeds are improved by roughly two orders of magnitude in relative infidelity, no seed has less than  $F = 0.97$ , and many solutions exceed the  $F = 0.99$  threshold. The fidelity distribution as a function of  $T$  is characteristically exponential, and for this batch we obtain the estimate  $T_{\text{qsl}}^{F=0.99} = 22.5$  ms with corresponding  $T_{\text{qsl}}^{F=0.99} = 11$  in simulation units. Based on the optimization trajectories shown in Fig. 5 we expect the existence of lower estimates since many optimizations ran out of wall time close to  $F = 0.99$  while still having a non-zero slope. The gain in fidelity per iteration is, however, exponentially diminishing with the optimization time.

For the same batch, Fig. 6 shows all the duration-

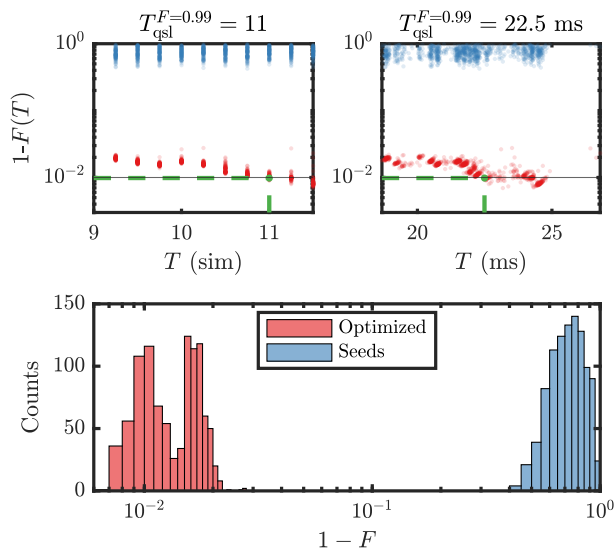


FIG. 4. Optimization results for a  $N_s = N_p = 20$  batch. Top row:  $1 - F$  (lower is better) for each seed before (blue dots) and after (red dots) optimization. The dot translucency informs about the distribution density. The results are plotted against transfer duration in both simulation and SI units. The SI conversions are obtained by Eq. (21) using  $J_x$  from Fig. 2, corresponding to the system parameters described at the end of Sec. III A. In this batch we find  $T_{\text{qsl}}^{F=0.99} = 22.5$  ms indicated with the green dashed line. Bottom row:  $1 - F$  histogram prior to and after optimization with the same color scheme.

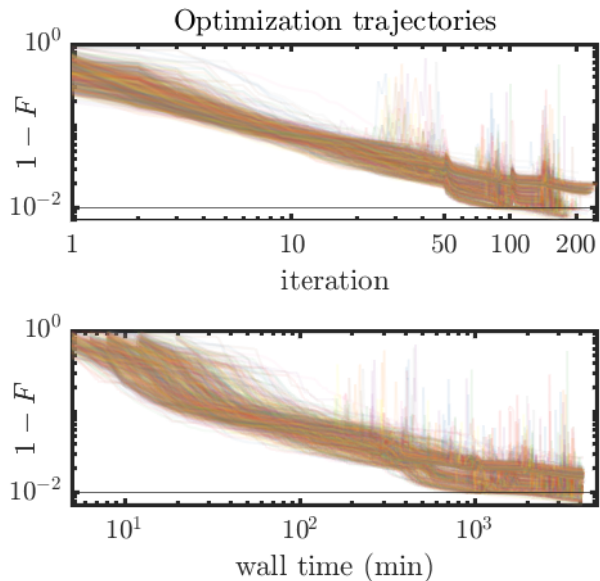


FIG. 5. Optimization trajectories. Each line shows  $1 - F$  as a function of iteration (top) and optimization wall time (bottom). Changes in the homotopy parameter  $\delta t$  manifest as kinks at 50 and 100 iterations (corresponding to  $\delta t$  changes  $0.1 \rightarrow 0.05$ , and  $0.05 \rightarrow 0.025$ ). Notably, a prominent dip in infidelity is seen at the first handover: the increased time resolution of the control allows more complex and fine-tuned dynamics. The homotopy approach accelerates the computations and roughly doubles the number of iterations achieved within the allocated time budget without sacrificing performance (the infidelity iteration trajectories follow roughly the same power-law for all three homotopy parameter regions).

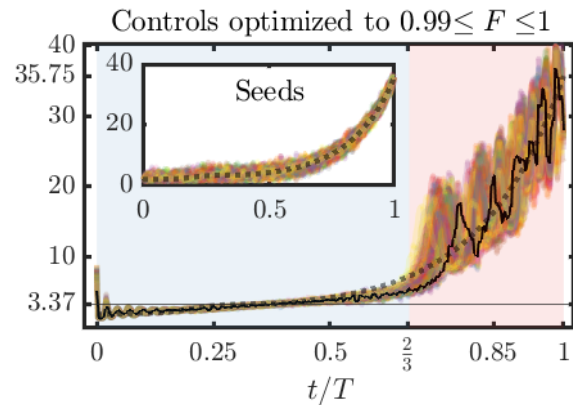


FIG. 6. Duration-normalized control ramps (multi-colored lines)  $u(t/T)$  for solutions with  $F \geq 0.99$ . The corresponding seeds are shown in the inset, the black dotted line indicates the adiabatic reference control, the horizontal black line denotes the critical point, and the black solid line highlights the optimal control with duration  $T_{\text{qsl}}^{F=0.99} = 22.5$  ms. The optimal controls are characterized by two distinct segments denoted by the blue and red shading.

normalized seed- and optimized controls ( $u(t/T)$ ) with final fidelities  $F \geq 0.99$ . From an initial qualitative visual inspection, the optimal controls are strikingly similar in structure, consisting of two characteristic ramp segments,

**Segment 1:**  $t/T \in [0, \frac{2}{3}]$ . With very low variance, we observe an initial high-frequency “wobble” that briefly exceeds the critical value for the phase transition, followed by slow, mainly linear crossing (see Fig. 2) overlaid with low amplitude, high frequencies.

**Segment 2:**  $t/T \in [\frac{2}{3}, 1]$ . The ramp shapes are dominated by lower frequencies, giving rise to a number of seemingly well-defined oscillations but with a more accentuated individual variance. As we show in the following, the underlying structure is in fact bang-bang on a linear background to which these oscillations are good approximations.

The physical significance of these segments are discussed later in this section. One possible explanation for the similarity of the optimized controls is that the seeding mechanism was not adequately exploratory, thus leading to the same attractor in the landscape upon optimization. It is, however, widely known that crossing the phase transition must typically be slow and deliberate such as to not pin residual defects in the atom number per site [31, 32, 76, 82], and we expect this to be reflected in some capacity also for time-optimal high-fidelity transfers. If this supposition is held as true, the seeds are in fact very exploratory in the first segment. The same is not true in the second segment where larger amplitudes are evidently more desirable. As in any optimal control problem, we note that it is entirely possible for the true optimal strategy not to be captured by the chosen seed-

ing mechanism. Nevertheless, robust structures emerge and we do not believe that e.g. simply increasing the seed amplitudes in the second segment would lead to identification of new strategies, but are rather likely to yield more rapid convergence to the ones we already identify in the following.

### A. Solution Strategies: Bang-Bang Structure

The bi-segmentation is not exclusive to  $F \geq 0.99$ , as virtually all optimized controls with  $F < 0.99$  (not shown) also exhibit the same overall structure: the first segments are almost exactly the same, but the first oscillation in the second segment is typically shifted slightly to  $t/T \approx 0.70$  and with much larger amplitudes as will also become clear momentarily. From the highlighted optimal control in Fig. 6 it is also evident that even the optimal controls do not all have the same frequency content in the second segment. For a quantitative study, we discard the first segment for each ramp, interpolate the remaining points on a 256 points grid, subtract a linear contribution (defined by the endpoints), and then subtract the value of the initial point. Figure 7 shows the result of applying this procedure to optimal and near-optimal controls at three different durations. With this we identify three distinct solution strategies that are active and optimal at different durations, each characterized by an integer number of oscillations:  $N_{\text{osc}} = 5, 6, 7$  at  $T = 9.25, 11, 11.5$ , respectively. In all instances, the first two oscillations are separated by roughly the same distance, the final oscillation has the same shape and location, and at least two penultimate oscillations overlap. We expect a smooth transition between the dominant strategy which can be interpreted as phase transitions of the optimization itself [54, 83]. Looking at the individual optimal and near-optimal controls at  $T = 11$ , we find that all  $N_{\text{osc}} = 5, 6, 7$  strategies are present, but with the majority belonging to  $N_{\text{osc}} = 6$  including the optimal control in Fig. 4. This is also why the median amplitude is overall less pronounced as some of the oscillation centers are offset. Similarly, but to less effect, we found  $N_{\text{osc}} = 6$  solutions at  $T = 9.25$  and  $T = 11.5$ .

Additionally, the individual oscillation amplitudes are also quite different in the three cases and the relatively larger amplitudes for the  $T = 9.25$  case in particular suggests that the underlying physical mechanism may in fact be a bang-bang structure (regions alternating between extremal values of the control) to which the observed oscillations are good approximations under the imposed regularizations penalties ( $\alpha = 10^{-7}$  and  $\gamma = 10^{-8}$ , leading to  $\langle J_\alpha \rangle = (7.4 \pm 0.6) \cdot 10^{-5}$  and  $\langle J_\gamma \rangle = (3.2 \pm 0.4) \cdot 10^{-4}$ ). By the same token, it is also possible that strategies with more or broader bangs exist even at these durations, but are not discovered due to the regularization. Noting that the full optimization landscape is  $J(\vec{u}) = J_F(\vec{u}) + J_\alpha(\vec{u}) + J_\gamma(\vec{u})$ , we provide the following possible interpretation as to why the  $T = 9.25$

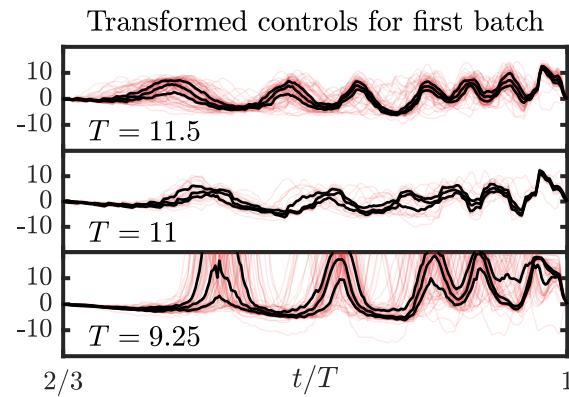


FIG. 7. Optimal ( $F \geq 0.99$ ) or near-optimal ( $F \geq 0.98$ ) controls (red lines) at three different durations after discarding the first segment, subtracting a linear contribution, and subsequently subtracting the resulting initial value. The control (25,50,75)% quantiles (black lines) show that relative abundance of the different strategies, each characterized by a number of oscillations or bangs, and the optimal one depends on  $T$ .

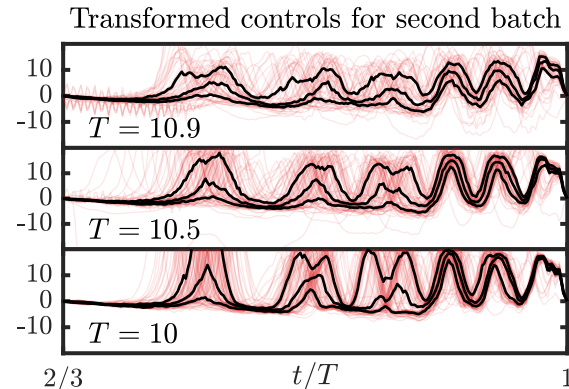


FIG. 8. Same as Fig. 7, but for the second optimization batch with 7 days of optimization time instead of 3, and at a different set of durations. The changing modality of the control quantiles reflect phase transitions in the optimization landscape.

exhibits the most clear bang-bang signature. First, if identification bangs (approximated by oscillations) are not themselves artifacts of the regularization costs, but truly due to the quantum dynamics encapsulated by the  $J_F$  term, this duration (fewest bangs) admits more rapid change and higher values per bang for the same cost value [84]. Second, the regularizations costs are not duration-normalized, again allowing both more rapid changes and to higher values for the same cost value. Third, the lower duration requires fewer time evolutions, allowing more iterations within the same optimization time as for the higher durations.

Based on the first batch of results discussed in Figs. 4-7 we expect that the true  $T_{\text{qsl}}^{F=0.99}$  is located in between  $T \in [9.25, 11]$  and that the time-optimal con-



trol(s) will likely belong to either the solution strategy with  $N_{\text{osc}} = 5$  or  $N_{\text{osc}} = 6$  bangs (or oscillation approximations thereof). To investigate this further, we ran another optimization batch in the duration interval  $T = [10, 10.1, \dots, 10.9]$ , this time allotting 7 days of wall time to each seed. For this batch we found better overall results, a better quantum speed limit estimate at  $T_{\text{qsl}}^{F=0.99} = 10.5$  (20.5 ms), and that the bang-bang structure was more pronounced. The same control bi-segmentation was identified, and in Fig. 8 we show the result of applying the same transformation procedure for the second segment as in the first batch. We observe that the medians are still associated with the  $N_{\text{osc}} = 6$  in all cases. However, whereas the last three quantile oscillations are relatively unchanged as  $T$  is lowered, the rest either split or merge. These changes in modality explicitly show the emergence of new prominent attractors in the optimization landscape, corresponding to the onset of new viable control strategies with a different number of bangs.

## B. Physical Interpretation of Optimal Controls and Benchmark Comparisons

Having established the notion of a general solution structure consisting of two distinct segments, we now turn to the dynamical evolution of observables and several figures of merit when propagated along a few particularly relevant controls: the optimal control found at  $T_{\text{qsl}}^{F=0.99} = 20.5$  ms in the second optimization batch, and two optimized controls at durations  $T = 14.9$  ms and  $T = 5.7$  ms that both have  $F < 0.99$  from a third optimization batch (3 days of optimization at a lower range of durations). The duration  $T = 14.9$  ms is significant because it approximately the duration at which the best figure merit  $\eta \approx 0.1$  was obtained in Ref. [32] (reabeled here as  $F_2 \rightarrow \eta$  for convenience), whereas  $T = 5.7$  ms is the lowest duration at which we obtain  $\eta \approx 0.1$ . This serves as a basis for both qualitative and quantitative comparisons to both Refs. [31]-[32]. Specifically, the additional figures of merit are the density of defects and the rescaled average variance,

$$\rho(t) = \frac{1}{N_s} \sum_{i=1}^{N_s} |\langle \hat{n}_i \rangle_{\psi(t)} - 1|, \quad \eta(t) = \frac{1}{N_s} \sum_{i=1}^{N_s} \frac{\Delta \hat{n}_i(t)}{\Delta \hat{n}_i(0)}, \quad (31)$$

where  $\langle \hat{n}_i \rangle_{\psi(t)} = \langle \psi(t) | \hat{n}_i | \psi(t) \rangle$  and  $\Delta \hat{n}_i(t) = \langle \hat{n}_i^2 \rangle_{\psi(t)} - \langle \hat{n}_i \rangle_{\psi(t)}^2$ . These were used as optimization objectives in Ref. [31] and Ref. [32], respectively, based on particular experimental setups and measurement capabilities, and in both instances, gradient-free methodologies were used to optimize the expansion coefficients of a chopped random basis of Fourier components (CRAB).

The three figures of merit (optimization objectives) possess vastly different relative leniency or strictness toward what qualifies as an optimal solution. For example,

$F = 0.99$  is very strict in that it requires nearly all the population to be in a single, well-defined state with fixed phase relations if it is spanned by more than a single Fock component. On the other hand, all site permutations of the states  $|1, 2, 2, 0, 0\rangle$ ,  $|1, 1, 3, 0, 0\rangle$ , and arbitrary normalized linear combinations thereof (both in magnitude and phase) yield the same  $\rho$ . As the system size is increased, the number of permutations increases drastically and with it the number of low-defect states that can be considered optimal with respect to e.g. the  $\rho = 10^{-3}$  threshold used in Ref. [31]. It strictly follows that optimality with respect to fidelity implies optimality with respect to  $\rho$ , but the relationship is unidirectional. A similar line of reasoning applies to  $\eta$  in Ref. [32]. Another concern with  $\rho$  and  $\eta$  in this application is that the acquired state will generally not be stationary by the same arguments. Typically, the creation of a Mott insulator is a preparation step in experiments, where one desires a setup of well-localized atoms for e.g. quantum simulation of spin chains or a quantum register for computation. If the final state is not stationary, it will start drifting while the actual experiment is taking place. By optimizing the ground state fidelity, we ensure that the resulting state remains stable throughout the remainder of the experimental cycle. Since the transfer occurs with respect to eigenstates of the Hamiltonian, a (nearly) equivalent quantity to fidelity is the diagonal entropy  $S_d = -\sum_i p_i \ln p_i$  [8], where  $p_i$  are the populations of the instantaneous energy eigenstates. This diagonal entropy is clearly minimized by  $S_d(\{p_i = 1; p_j = 0, j \neq i\})$  and thus also for the ground state  $i = 0$ , which is likely, but not necessarily, the closest attractor whenever the initial guess yields a non-vanishing fidelity. In any event, stricter requirements necessarily leads to both comparatively increased time scales for optimality, overall problem difficulty, and most likely complexity of the optimal solutions.

Figure 9 shows the propagation results for the three optimized controls. In all instances, the fidelity is basically unchanged during the first ramp segment ( $2/3 \geq t/T$ , crossing the phase transition) whereas the decreasing  $\rho(t)$  and  $\eta(t)$  reflects the light-cone-like rearrangement of site population  $\langle \hat{n}_i \rangle_{\psi(t)}$  initially concentrated in the bulk (roughly sites 4 – 17) due to finite edge effects. The bulk depletion is relatively homogeneous for  $T_{\text{qsl}}^{F=0.99} = 20.5$  ms, whereas inhomogeneous low-density ripples emanate from both edges until converging at the center for  $T = 14.9$  ms. For  $T = 5.6$  ms, the ripple inhomogeneity is much more severe and the propagation speed is too slow to reach the center at this duration. Clearly, the propagation velocity  $\partial \langle \hat{n}_i \rangle / \partial t$  is a limiting process for the achievable quantum speed limits. During the second ramp segment ( $2/3 \leq t/T$ , well-defined bangs to the maximum value imposed on a line), the infidelity  $1 - F$  drops dramatically alongside  $\rho(t)$  and  $\eta(t)$ . During the bangs, tunneling events are approximately negligible  $\hat{H}_n \approx \hat{H}_n^c$ , briefly pinning the atoms (e.g. nearly no change in fidelity) and imprinting a  $c$ -number phase on

each state component,

$$\hat{\mathcal{U}}_n |n_1, \dots, n_{N_s}\rangle \approx e^{-\frac{i u_n^{\max} \delta t}{2} \sum_{i=1}^{N_s} n_i(n_i-1)} |n_1, \dots, n_{N_s}\rangle, \quad (32)$$

for each time step  $\delta t$  of the bang. Outside the bangs, tunneling resumes. The bangs are thus associated with phase adjustments necessary for following quantum interference pathways leading to high-fidelity results. This is a complex process as revealed by the highly non-monotonic behavior of the fidelity for the optimal control at  $T_{\text{qsl}}^{F=0.99} = 20.5$  ms, where five bangs (or approximations thereof) are visible. At  $T = 14.9$  ms, four bangs are clearly identified, and at  $T = 5.7$  ms only a single bang is present.

The minimum value for each figure of merit during the transfers is shown in Table II. From this data we find that each achieved figure of merit is worsened by an order of magnitude as the duration is decreased, and it is clear that even very poor fidelities can yield competitive quantitative results in terms of  $\eta$  and  $\rho$  compared to the benchmark Refs. [31]-[32]. Assuming that the relationship between the orders of magnitude is a general one, results similar to the  $T = 14.9$  ms case are obtained in Fig. 4 with just 10 iterations or correspondingly roughly an hour of optimization time. Additionally, in rough numbers, we find solutions that matches the best result in Ref. [32] at  $T = 5.7$  ms, a third of the duration. For optimal fidelities  $F = 0.99$ , the other figure of merits are comparatively lower by orders of magnitude compared to the benchmarks' due to the unidirectional relationship. In all instances, these performance gaps would increase further if  $\eta$  or  $\rho$  was directly subject to exact derivative-based optimizations, and it is reasonable to assume that the comparative conclusions would remain true if our methodologies were applied to exactly the same problem parameters.

From a qualitative point of view, the optimized controls obtained in Refs. [31]-[32] are very smooth by construction, which is in stark contrast to the general bang structure identified throughout this work. In other words, the obtained optimized controls have a higher information-theoretic *control complexity* as initially introduced in Ref. [8], where an operational definition is given by the number of Fourier components needed to solve the problem to a given fidelity threshold (these and associated notions were shortly after treated in more generality in Ref. [58]). Apart from the difference in optimization objective, this may also be due to the truncation parameters for the matrix product states therein ( $D \leq 100$  and  $D \leq 24$ ,  $s_{\max} = 10^{-5}$ , respectively) corresponding to a more approximate, low-entanglement representation of the model. It is, however, satisfactory to note that these smoother controls still possess a virtually identical bi-segmentational structure, and that their rapid increase in the second segment can in a sense be interpreted as approximately a single bang resembling Fig. 9 which is sufficient for reducing the more lenient

| $T$ (ms) | $1 - F$             | $\rho$              | $\eta$              |
|----------|---------------------|---------------------|---------------------|
| 20.5     | $1.0 \cdot 10^{-2}$ | $2.4 \cdot 10^{-4}$ | $4.1 \cdot 10^{-3}$ |
| 14.9     | $0.7 \cdot 10^{-1}$ | $2.1 \cdot 10^{-3}$ | $1.9 \cdot 10^{-2}$ |
| 5.7      | $0.4 \cdot 10^0$    | $1.9 \cdot 10^{-2}$ | $0.9 \cdot 10^{-1}$ |

TABLE II. Minimal figure of merit values from Fig. 9, optimized for fidelity. For reference, the best achieved result reported in Refs. [31]-[32] are  $\rho = 10^{-3}$  and  $\eta = 10^{-1}$ , respectively optimized for in similar systems.

figures of merit to below the specific measurement resolution in Ref. [32]. It is also remarked in Ref. [31] that  $D > 50$  did not significantly change the objective value.

Finally, we have also run a preliminary fourth optimization batch at durations beyond  $T_{\text{qsl}}^{F=0.99}$  with different combinations of lowered regularization strengths  $\gamma, \alpha = 10^{-8} - 10^{-10}$  and three days of optimization time with a reduced number of seeds. At each duration we find a similar, continued exponential behavior of the best achieved fidelity with many solutions at e.g.  $T_{\text{qsl}}^{F=0.999} = 16.5$  (34.2 ms) and  $T_{\text{qsl}}^{F=0.9998} = 21$  (44 ms), many of which are still not converged, very nearly closing in on  $T_{\text{qsl}}^{F=0.9999}$  solutions. However, we also find i) the bangs remains attenuated similar to Fig. 6, but more severely and ii) the emergence of low to vanishing fidelity attractors, corresponding to controls that are very irregular and structureless. Under the current seeding strategy and supposition that the identified bang-bang structure for the second segment remains the true optimal strategy also at these durations, both i) and ii) illuminates a highly non-trivial balancing of the terms because of the very different behavior in the two segments. A possible avenue for further investigation is provided in the outlook, and we expect existence of solutions at those thresholds with somewhat lower durations.

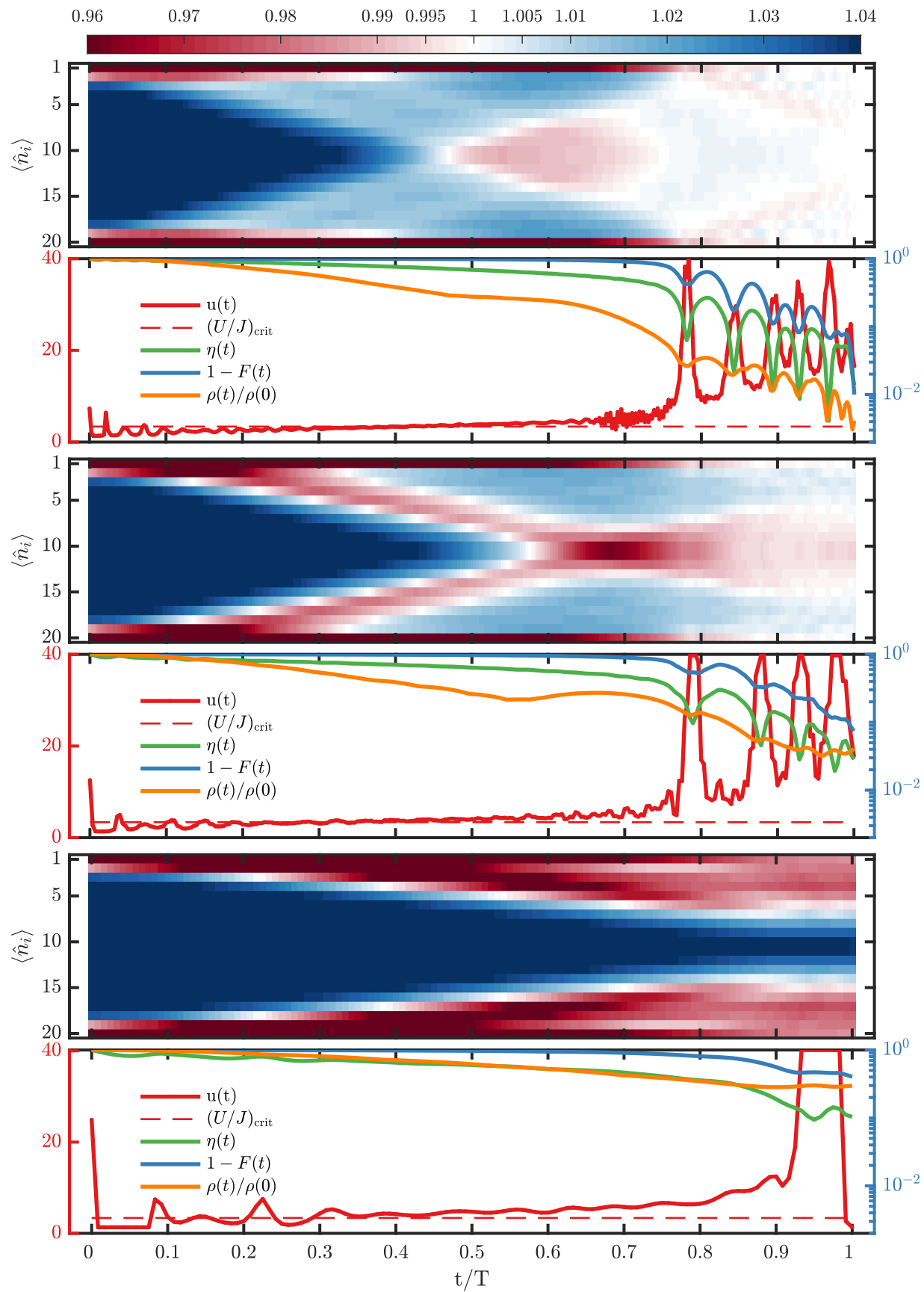


FIG. 9. Time evolution of the initial state along the optimal control at  $T_{\text{qsl}}^{F=0.99} = 20.5\text{ms}$  (top) and optimized controls at  $T = 14.9\text{ms}$  (middle) and  $T = 5.7\text{ms}$  (bottom). Each case shows site occupations  $\langle \hat{n}_i \rangle_{\psi(t)}$  with a color scale sensitive to near-unit values (the outer site occupancy is initially 0.67) as well the control (red axis) and figures of merit (blue axis) defined in text during the evolution. Note the density of defects is normalized to its initial value ( $\rho(0) = 6.7 \cdot 10^{-2}$ ) in this figure.

## V. CONCLUSION AND OUTLOOK

We discussed how and why accurate derivatives are central to achieve high fidelities and convergence rates in derivative-based methods for generic optimization tasks. We examined three common choices of time evolution scheme, the exact- and two second-order Suzuki-Trotter expanded propagators, showed how these can be interpreted and related in terms of optimization landscapes, and found by novel calculations their resulting analytically exact derivatives to differ vastly in complexity. By assuming a diagonal control Hamiltonian for the Trotterized landscape, we circumvented a detrimental infinite series, and highlighted many additional attractive properties compared to the exact landscape, among others the extended range of applicability with respect to system size. In a certain sense, when balancing respective errors in the dynamics and in the derivative calculations, the latter is more important. We demonstrated the main ideas first by considering a minimal LZ problem, which has certain similarities to the many-body arena, and then applied the methodology to a genuine many-body problem described by matrix product states where exact propagation is impossible. In both instances, the exact derivatives lead to the expected rapid convergence rates and high-fidelity results (unit to machine precision and 0.99-0.9999, respectively). For the many-body case, we compared and built upon earlier seminal work that proved experimental feasibility using a gradient-free approach on more lenient figures of merit and found significant improvements in all performance metrics, transformation times, and a wholly different structure of the optimized controls (bang-bang as opposed to smooth). The demonstrated efficiency in both extremes of Hilbert space dimensionality suggests that these exact derivative methodologies could potentially be useful in applications across the range of research areas listed in Sec. I.

We now turn to mentioning a few possible areas for future study.

The exact Hessian has strong theoretical properties as discussed in Sec. II, and although our calculations of the exact Hessian have been verified numerically, we found its use to be limited for the particular set of parameters defining the Bose-Hubbard problem: on a per-iteration basis, the relative gain was far outweighed by the increase in computation time due to scaling properties. Nevertheless, we have found in a parallel, similar work that the exact Hessian for unitary gate synthesis (manuscript in preparation) outperforms a gradient-only quasi-Newton approach in terms of statistics and best results in certain domains. This highly suggests similar possibilities in the present case, which could for example either be investigated in the toy problem from Sec. II or in smaller Bose-Hubbard system sizes  $N_s = N_p \leq 5$ .

The inclusions of a maximal control amplitude and regularizations are rooted in experimental limitations of throughput and switching times. However, the bang-

bang structure was found to be increasingly washed out and emergence of low fidelity solutions at longer durations, both most likely due to the somewhat arbitrarily chosen regularization strength parameters. We also note that the upper control bound value was imposed somewhat arbitrarily close to the value defining the target state. Since the atoms are already site locked at this value, increasing the bound would simply accelerate the phase accumulation in Eq. (32), which may allow faster transfers. In the event of an actual experimental implementation, they would have to be consistent with the pertinent limitations of the given setup for example by taking into account the transfer function of the electronics, although additional study of these hyperparameter values could prove beneficial on their own right. One possible direction is the following.

Based on the bi-segmentational findings for the  $N_s = N_p = 20$  Bose-Hubbard state transfer, we may conjecture an associated reduced control problem with a specialized seeding strategy as follows: i) take as initial state  $|\psi_{\text{ini}}\rangle = \hat{U}_{\text{seg},1}^{\text{ST}}(\frac{2}{3}T; 0)|\text{SF}\rangle$  for the optimization, where  $\hat{U}_{\text{seg},1}^{\text{ST}}(\frac{2}{3}T; 0)$  is the propagator over the first ramp segment for e.g. the  $T_{\text{qsl}}^{F=0.99}$  solution, and ii) optimize the second segment,  $|\psi(T)\rangle = \hat{U}_{\text{seg},2}^{\text{ST}}(T; \frac{2}{3}T)|\psi_{\text{ini}}\rangle$ , where the seeding strategy entails an explicit bang-bang structure. The optimization could proceed either on the control values themselves, or maybe even more interestingly, on the set of parameters defining the bangs, i.e. their widths, heights, location. This is similar to a chopped random basis function decomposition approach [40, 44, 85]. Since time evolution constitutes the main time consumption for optimizations, a relative factor 3 increase in the total number of iterations performed for the same wall times is expected (because effectively only one third of the original duration is now optimized). This increases the likelihood of locating a lower  $T_{\text{qsl}}$ . The relative success of such an approach may be warranted only because the first segment has low to zero variance, which is *a priori* non-trivial. It follows that the state trajectories in Hilbert space are similar or identical for large portions of the transfer. The proposed reduced problem effectively enforces the optimal trajectories to pass through the points along this path, which is a very strong imposition. For the control problem studied in Ref. [86] it was found that a similarly reduced problem was detrimental to acquiring low  $T_{\text{qsl}}^{F=0.99}$  estimates. In this case, however, the propensity for *all* optimizations to yield the same initial ramp behavior suggests that the reduced problem may be a sufficient representation for the full problem and can be studied with relative impunity. If this is not the case, another possible scheme would be to alternate between optimizing the full and reduced problems, or have different parameterizations or seeding strategies for the two segments individually. This may also elucidate and more readily drive an extended study of the control strategies emerging as the transfer duration is altered. A further treatment and characterization of the control strategies



and their hierarchy in the vein of Ref. [54] would be interesting. In addition, such optimal strategy analysis could also be connected to the information-theoretic control complexity notions [8, 58] discussed in Sec. IV, both as a function of system size and duration.

Our optimizations did not explicitly include robustness criteria to e.g. the number of particles present in the system, which is realistic in an experimental setting. By defining an average cost function over e.g.  $N_p = 18, 19, 20, 21, 22$  and optimizing with the ensuing average gradient, one would obtain controls with built-in robustness towards such fluctuations.

### Appendix A: Derivation of Exact Gradients and Hessians

Here we present the calculations leading to the exact gradient and Hessian expressions for both the exact propagator and the Trotterized propagators with a diagonal control Hamiltonian defined in Eqs. (6)-(8). We also define the regularization cost functionals and calculate likewise calculate their derivatives after discretization. Emphasis is put on thoroughness of the steps, and relevant equations for the derivations are re-stated for convenience where applicable, so as to be self-contained.

We assume a piecewise constant control  $u(t)$  on a regularly spaced time grid  $t \in [t_1, t_2, \dots, t_{N_t}] = [0, \delta t, \dots, T]$ . Recall  $|\psi_1\rangle = |\psi_{\text{ini}}\rangle$  and  $|\psi_{N_t}\rangle = |\psi(T)\rangle$ , and  $\hat{H}(u_n) = \hat{H}_n = \hat{H}_n^d + \hat{H}_n^c$  where  $\hat{H}_n^c$  ( $\hat{H}_n^d$ ) is the control (drift) Hamiltonian. Define the auxiliary state  $|\chi_{N_t}\rangle = |\psi_{\text{tgt}}\rangle$ , the transfer amplitude  $o = \langle \psi_{\text{tgt}} | \psi(T) \rangle = \langle \chi_{N_t} | \psi_{N_t} \rangle$ .

#### 1. Derivatives for Exact Propagator

The exact propagator has the form  $\hat{\mathcal{U}}_n = \exp(-i\hat{H}(u_n)\delta t)$  where the <sup>Ex</sup> superscript is omitted for brevity in most of the steps. It is convenient to write

$$F = |\langle \psi_{\text{tgt}} | \psi(T) \rangle|^2 = o^* o, \quad (\text{A1})$$

$$\frac{\partial J_F^{\text{Ex}}}{\partial u_n} = -\Re \left( o^* \frac{\partial o}{\partial u_n} \right), \quad (\text{A2})$$

with the overlap  $o$  and its derivative being

$$o = \langle \psi_{\text{tgt}} | \psi(T) \rangle = \left\langle \chi_{N_t} \left| \hat{\mathcal{U}}_{N_t-1} \dots \hat{\mathcal{U}}_n \dots \hat{\mathcal{U}}_1 \right| \psi_1 \right\rangle, \quad (\text{A3})$$

$$\frac{\partial o}{\partial u_n} = \left\langle \chi_{N_t} \left| \hat{\mathcal{U}}_{N_t-1} \dots \frac{\partial \hat{\mathcal{U}}_n}{\partial u_n} \dots \hat{\mathcal{U}}_1 \right| \psi_1 \right\rangle \quad (\text{A4})$$

$$= \left\langle \chi_{n+1} \left| \frac{\partial \hat{\mathcal{U}}_n}{\partial u_n} \right| \psi_n \right\rangle. \quad (\text{A5})$$

The task is then to calculate  $\frac{\partial \hat{\mathcal{U}}_n}{\partial u_n}$  and be careful with ordering. Define the control derivative  $H'_n \equiv \frac{\partial \hat{H}_n}{\partial u_n}$  and expand the exponential

$$\begin{aligned} \frac{\partial \hat{\mathcal{U}}_n}{\partial u_n} &= \frac{\partial}{\partial u_n} \left( e^{-i\hat{H}_n \delta t} \right) = \sum_{p=0}^{\infty} \frac{(-i\delta t)^p}{p!} \frac{\partial}{\partial u_n} \left( \hat{H}_n^p \right) \\ &= \sum_{p=1}^{\infty} \frac{(-i\delta t)^p}{p!} \sum_{q=0}^{p-1} \hat{H}_n^q \hat{H}'_n \hat{H}_n^{p-q-1}, \end{aligned} \quad (\text{A6})$$

Define for momentary simplicity  $A \equiv -i\hat{H}_n \delta t$  and  $B \equiv -i\hat{H}'_n \delta t$ . Then it can be shown that

$$\frac{\partial \hat{\mathcal{U}}_n}{\partial u_n} = \sum_{p=0}^{\infty} \sum_{q=0}^{\infty} \frac{A^p B A^q}{(p+q+1)!}. \quad (\text{A7})$$

Using now the following relations for the Beta and Gamma functions [87]:

$$\Gamma(a) = (n-1)! \quad (\text{for } a \in \mathbb{Z}^+), \quad (\text{A8})$$

$$\begin{aligned} \beta(a, b) &= \int_0^1 (1-\alpha)^{a-1} \alpha^{b-1} d\alpha = \frac{\Gamma(a)\Gamma(b)}{\Gamma(a+b)} \\ &= \frac{(a-1)!(b-1)!}{(a+b-1)!} = \frac{p!q!}{(p+q+1)!}, \end{aligned} \quad (\text{A9})$$

and taking  $a = p+1$ ,  $b = q+1$  we obtain

$$\frac{1}{(p+q+1)!} = \frac{1}{p!q!} \int_0^1 (1-\alpha)^p \alpha^q d\alpha. \quad (\text{A10})$$

Inserting this, and initially pulling out the integral we obtain

$$\begin{aligned} \frac{\partial \hat{\mathcal{U}}_n}{\partial u_n} &= \sum_{p=0}^{\infty} \sum_{q=0}^{\infty} \frac{A^p B A^q}{p!q!} \int_0^1 \alpha^p (1-\alpha)^q d\alpha \\ &= \int_0^1 \left( \sum_{p=0}^{\infty} \frac{((1-\alpha)A)^p}{p!} \right) B \sum_{q=0}^{\infty} \frac{(\alpha A)^q}{q!} d\alpha \\ &= \int_0^1 e^{(1-\alpha)A} B e^{\alpha A} d\alpha = e^A \int_0^1 e^{-\alpha A} B e^{\alpha A} d\alpha \\ &= \hat{\mathcal{U}}_n \int_0^1 e^{(i\alpha\delta t)\hat{H}_n} (-i\delta t \hat{H}'_n) e^{-(i\alpha\delta t)\hat{H}_n} d\alpha. \end{aligned} \quad (\text{A11})$$

The integrand can be evaluated by defining the recursive commutator with base case  $[c_x X, c_y Y]_0 = c_y Y$  as in the main text and using Baker-Campbell-Hausdorff relations [88]

$$[c_x X, c_y Y]_k = [c_x X, [c_x X, c_y Y]_{k-1}] = c_x^k c_y [X, Y]_k, \quad (\text{A12})$$

$$e^{c_x X} Y e^{-c_x X} = \sum_{k=0}^{\infty} \frac{[c_x X, c_y Y]_k}{k!} = \sum_{k=0}^{\infty} \frac{c_x^k c_y}{k!} [X, Y]_k, \quad (\text{A13})$$

by evaluating these with scalars  $c_x = i\alpha\delta t$  and  $c_y = -i\delta t$

$$\begin{aligned}\frac{\partial \hat{\mathcal{U}}_n}{\partial u_n} &= \hat{\mathcal{U}}_n \int_0^1 \left( \sum_{k=0}^{\infty} \frac{(i\alpha\delta t)^k (-i\delta t)}{k!} [\hat{H}_n, \hat{H}'_n]_k d\alpha \right) \\ &= \hat{\mathcal{U}}_n \sum_{k=0}^{\infty} (-i\delta t) \frac{i^k \delta t^k}{k!} [\hat{H}_n, \hat{H}'_n]_k \left( \int_0^1 \alpha^k d\alpha \right) \\ &= \hat{\mathcal{U}}_n (-i\delta t) \sum_{k=0}^{\infty} \frac{i^k \delta t^k}{(k+1)!} [\hat{H}_n, \hat{H}'_n]_k. \quad (\text{A14})\end{aligned}$$

Substituting this into Eq. (A5), the resulting expression into Eq. (A2), and using  $\hat{H}'_n = \hat{H}'_n{}^{c'}$  gives

$$\begin{aligned}\frac{\partial J_F^{\text{Ex}}}{\partial u_n} &= \Re \left( i o^* \left\langle \chi_n \left| \left( \sum_{k=0}^{\infty} \frac{i^k \delta t^k}{(k+1)!} [\hat{H}_n, \hat{H}'_n{}^{c'}]_k \right) \right| \psi_n \right\rangle \right) \delta t \\ &= \Re \left( i o^* \left\langle \chi_n \left| \hat{H}'_n{}^{c'} \right| \psi_n \right\rangle \right) \delta t + \mathcal{O}_{\nabla J_F}(\delta t^2). \quad (\text{A15})\end{aligned}$$

which is the expression stated in (11).

To calculate the Hessian, we take the derivative of Eq. (A2)

$$\frac{\partial^2 J_F^{\text{Ex}}}{\partial u_n \partial u_m} = -\Re \left( \left( \frac{\partial o}{\partial u_m} \right)^* \frac{\partial o}{\partial u_n} + o^* \frac{\partial^2 o}{\partial u_n \partial u_m} \right). \quad (\text{A17})$$

This form is valid for both the exact and Trotterized propagator. We recall previous definitions with an additional index  $m$  highlighted:

$$o = \langle \chi_{N_t} | \hat{\mathcal{U}}_{N_t-1} \dots \hat{\mathcal{U}}_n \dots \hat{\mathcal{U}}_m \dots \hat{\mathcal{U}}_1 | \psi_1 \rangle, \quad (\text{A18})$$

$$\begin{aligned}\frac{\partial o}{\partial u_n} &= \langle \chi_{N_t} | \hat{\mathcal{U}}_{N_t-1} \dots \frac{\partial \hat{\mathcal{U}}_n}{\partial u_n} \dots \hat{\mathcal{U}}_m \dots \hat{\mathcal{U}}_1 | \psi_1 \rangle \\ &= \langle \chi_{n+1} | \frac{\partial \hat{\mathcal{U}}_n}{\partial u_n} | \psi_n \rangle. \quad (\text{A19})\end{aligned}$$

With the gradient at hand, the Hessian calculation thus only needs additional evaluation of the second derivatives of  $o$ ,

$n > m :$

$$\begin{aligned}\frac{\partial^2 o}{\partial u_n \partial u_m} &= \langle \chi_{N_t} | \hat{\mathcal{U}}_{N_t-1} \dots \frac{\partial \hat{\mathcal{U}}_n}{\partial u_n} \dots \frac{\partial \hat{\mathcal{U}}_m}{\partial u_m} \dots \hat{\mathcal{U}}_1 | \psi_1 \rangle \\ &= \langle \chi_{n+1} | \frac{\partial \hat{\mathcal{U}}_n}{\partial u_n} \left( \prod_{j=m+1}^{n-1} \hat{\mathcal{U}}_j \right) \frac{\partial \hat{\mathcal{U}}_m}{\partial u_m} | \psi_m \rangle, \quad (\text{A20a})\end{aligned}$$

$n = m :$

$$\begin{aligned}\frac{\partial^2 o}{\partial u_n \partial u_m} &= \langle \chi_{N_t} | \hat{\mathcal{U}}_{N_t-1} \dots \frac{\partial^2 \hat{\mathcal{U}}_n}{\partial u_n^2} \dots \hat{\mathcal{U}}_1 | \psi_1 \rangle \\ &= \langle \chi_{n+1} | \frac{\partial^2 \hat{\mathcal{U}}_n}{\partial u_n^2} | \psi_n \rangle. \quad (\text{A20b})\end{aligned}$$

The case  $m > n$  is the same as  $n > m$  with indices  $n \rightleftharpoons m$  (we need only calculate one of the cases due to

symmetricity). Inserting these expressions in Eq. (A17) we obtain the exact Hessian elements  $n \geq m$  (without loss of generality) for the exact propagator

$$\begin{aligned}\frac{\partial^2 J_F^{\text{Ex}}}{\partial u_n \partial u_m} &= -\Re \left( \langle \psi_m | \frac{\partial \hat{\mathcal{U}}_m}{\partial u_m} | \chi_{m+1} \rangle \langle \chi_{n+1} | \frac{\partial \hat{\mathcal{U}}_n}{\partial u_n} | \psi_n \rangle \right) \\ &\quad - \Re \left( o^* \langle \chi_{n+1} | \frac{\partial \hat{\mathcal{U}}_n}{\partial u_n} \left( \prod_{j=m+1}^{n-1} \hat{\mathcal{U}}_j \right) \frac{\partial \hat{\mathcal{U}}_m}{\partial u_m} | \psi_m \rangle \right) (1 - \delta_{n,m}) \\ &\quad - \Re \left( o^* \langle \chi_{n+1} | \frac{\partial^2 \hat{\mathcal{U}}_n}{\partial u_n^2} | \psi_n \rangle \right) \delta_{n,m} \quad (\text{A21})\end{aligned}$$

where  $\frac{\partial \hat{\mathcal{U}}_n}{\partial u_n}$  is given by Eq. (A14). Evaluating  $\frac{\partial^2 \hat{\mathcal{U}}_n}{\partial u_n^2}$  is straightforward,

$$\begin{aligned}\frac{\partial^2 \hat{\mathcal{U}}_n}{\partial u_n^2} &= \hat{\mathcal{U}}_n \left\{ \left( -i\delta t \sum_{k=0}^{\infty} \frac{i^k \delta t^k}{(k+1)!} [\hat{H}_n, \hat{H}'_n]_k \right)^2 \right. \\ &\quad \left. - i\delta t \sum_{k=0}^{\infty} \frac{i^k \delta t^k}{(k+1)!} [\hat{H}_n, \hat{H}'_n]_k \right\}, \quad (\text{A22})\end{aligned}$$

but the recursive commutator derivative is cumbersome

$$\begin{aligned}[\hat{H}_n, \hat{H}'_n]_k &= [\hat{H}_n, [\hat{H}_n, \hat{H}'_n]_{k-1}] - [\hat{H}'_n, [\hat{H}_n, \hat{H}'_n]_{k-1}] \\ &\quad (\text{A23a}) \\ [\hat{H}_n, \hat{H}'_n]_0 &= \hat{H}_n'', \\ [\hat{H}_n, \hat{H}'_n]_1 &= [\hat{H}_n, \hat{H}_n''], \\ [\hat{H}_n, \hat{H}'_n]_2 &= [\hat{H}_n, [\hat{H}_n, \hat{H}_n'']] + [\hat{H}'_n, [\hat{H}_n, \hat{H}_n'']], \\ &\quad \vdots\end{aligned}$$

where we explicitly evaluated the first few terms. Note that the exact derivatives both entail an infinite summation (machine precision in finite arithmetic).

## 2. Derivatives for Trotterized Propagators

We consider now in turn the Suzuki-Trotter expansions  $\hat{\mathcal{U}}_n^{\text{ST}_1} = \hat{\mathcal{U}}_{n+1}^{c/2} \hat{\mathcal{U}}_n^d \hat{\mathcal{U}}_n^{c/2}$  and  $\hat{\mathcal{U}}_n^{\text{ST}_2} = \hat{\mathcal{U}}_n^{c/2} \hat{\mathcal{U}}_n^d \hat{\mathcal{U}}_n^{c/2}$  where  $\hat{\mathcal{U}}_n^{c/2} \equiv e^{-i\hat{H}_n^c \delta t/2}$  and  $\hat{\mathcal{U}}_n^d \equiv e^{-i\hat{H}_n^d \delta t}$ .

### a. Derivatives of $\hat{\mathcal{U}}_n^{\text{ST}_1}$

For the Suzuki-Trotter expansion  $\hat{\mathcal{U}}_n^{\text{ST}} = \hat{\mathcal{U}}_{n+1}^{c/2} \hat{\mathcal{U}}_n^d \hat{\mathcal{U}}_n^{c/2}$  the control dependence is distributed among  $n$  and  $n-1$  (except at the end points  $n=1, N$ ), yielding

$$\frac{\partial J_F^{\text{ST}_1}}{\partial u_n} = -\Re \left( o^* \frac{\partial o}{\partial u_n} \right), \quad (\text{A24a})$$

$$\frac{\partial o}{\partial u_n} = \left\langle \chi_{n+1} \left| \frac{\partial}{\partial u_n} \left( \hat{\mathcal{U}}_n^{\text{ST}_1} \hat{\mathcal{U}}_{n-1}^{\text{ST}_1} \right) \right| \psi_{n-1} \right\rangle. \quad (\text{A24b})$$

Additionally, assume that the control Hamiltonian is diagonal. We use Eq. (A14) to take the derivative of  $(\hat{U}_n^{\text{ST}_1} \hat{U}_{n-1}^{\text{ST}_1})$ ,

$$\begin{aligned} \frac{\partial}{\partial u_n} (\hat{U}_n^{\text{ST}_1} \hat{U}_{n-1}^{\text{ST}_1}) &= \frac{\partial}{\partial u_n} \left( (\hat{U}_{n+1}^{c/2} \hat{U}_n^d \hat{U}_n^{c/2}) (\hat{U}_n^{c/2} \hat{U}_{n-1}^d \hat{U}_{n-1}^{c/2}) \right) \\ &= (\hat{U}_{n+1}^{c/2} \hat{U}_n^d) \frac{\partial \hat{U}_n^c}{\partial u_n} (\hat{U}_{n-1}^d \hat{U}_{n-1}^{c/2}) \\ &= (\hat{U}_{n+1}^{c/2} \hat{U}_n^d) \left\{ \hat{U}_n^c (-i\delta t \hat{H}_n^{c'}) \right\} (\hat{U}_{n-1}^d \hat{U}_{n-1}^{c/2}) \\ &= (-i\delta t) \cdot (\hat{U}_{n+1}^{c/2} \hat{U}_n^d \hat{U}_n^{c/2}) \hat{H}_n^{c'} (\hat{U}_n^{c/2} \hat{U}_{n-1}^d \hat{U}_{n-1}^{c/2}) \\ &= (-i\delta t) \cdot \hat{U}_n^{\text{ST}_1} \hat{H}_n^{c'} \hat{U}_{n-1}^{\text{ST}_1}. \end{aligned} \quad (\text{A25})$$

Here we also used that two diagonal matrices always commute, first to evaluate the recursive commutator  $[\hat{H}_n^c, \hat{H}_n^{c'}]_k = \hat{H}_n^{c'} \cdot \delta_{0,k}$  from (A14), and second to recombine the initial propagators since  $[\hat{H}_n^{c'}, \hat{U}_n^{c/2}] = 0$ . Inserting into (A24a)-(A24b) yields the exact gradient stated in Eq. (12),

$$\frac{\partial J_F^{\text{ST}}}{\partial u_n} = \Re \left( i o^* \left\langle \chi_n \left| H_n^{c'} \right| \psi_n \right\rangle \right) \delta t, \quad (\text{A26})$$

with an additional factor 1/2 at the end points ( $n = 1, N_t$ ). Apart from these, this is identical to exact propagator gradient Eq. (11) when in the first-order approximation  $k_{\text{max}} = 0$ , i.e. discarding the otherwise expensive  $\mathcal{O}(\delta t^2)$  tail.

The Hessian elements are written as

$$\frac{\partial^2 J_F}{\partial u_n \partial u_m} = -\Re \left( \left( \frac{\partial o}{\partial u_m} \right)^* \frac{\partial o}{\partial u_n} + o^* \frac{\partial^2 o}{\partial u_n \partial u_m} \right). \quad (\text{A27})$$

The second derivatives to be calculated are

$n > m$ :

$$\begin{aligned} \frac{\partial^2 o}{\partial u_n \partial u_m} &= \langle \chi_{n+1} | \frac{\partial}{\partial u_n} (\hat{U}_n^{\text{ST}} \hat{U}_{n-1}^{\text{ST}}) \\ &\quad \left( \prod_{j=m+1}^{n-2} \hat{U}_j \right) \frac{\partial}{\partial u_m} (\hat{U}_m^{\text{ST}} \hat{U}_{m-1}^{\text{ST}}) | \psi_{m-1} \rangle, \end{aligned} \quad (\text{A28a})$$

$n = m$ :

$$\frac{\partial^2 o}{\partial u_n \partial u_m} = \langle \chi_{n+1} | \frac{\partial^2}{\partial u_n^2} (\hat{U}_n^{\text{ST}} \hat{U}_{n-1}^{\text{ST}}) | \psi_{n-1} \rangle. \quad (\text{A28b})$$

For  $n > m$  we only need the first derivative given in Eq. (A25). For  $n = m$  we take the second derivative of  $(\hat{U}_n^{\text{ST}} \hat{U}_{n-1}^{\text{ST}})$  using Eq. (A25) and commutation relations

due to diagonal  $H_n^c$

$$\begin{aligned} \frac{\partial^2}{\partial u_n^2} (\hat{U}_n^{\text{ST}} \hat{U}_{n-1}^{\text{ST}}) &= (-i\delta t) \frac{\partial}{\partial u_n} (\hat{U}_n^{\text{ST}} \hat{H}_n^{c'} \hat{U}_{n-1}^{\text{ST}}) \\ &= (-i\delta t) \hat{U}_{n+1}^{c/2} \hat{U}_n^d \frac{\partial}{\partial u_n} (\hat{U}_n^c \hat{H}_n^{c'}) \hat{U}_{n-1}^d \hat{U}_{n-1}^{c/2} \\ &= (-i\delta t) \hat{U}_{n+1}^{c/2} \hat{U}_n^d \left( \hat{U}_n^c (-i\delta t \hat{H}_n^{c'}) \hat{H}_n^{c'} + \hat{U}_n^c \hat{H}_n^{c''} \right) \hat{U}_{n-1}^d \hat{U}_{n-1}^{c/2} \\ &= (-i\delta t) \hat{U}_{n+1}^{c/2} \hat{U}_n^d \hat{U}_n^{c/2} \left( \hat{H}_n^{c''} - i\delta t (\hat{H}_n^{c'})^2 \right) \hat{U}_n^{c/2} \hat{U}_{n-1}^d \hat{U}_{n-1}^{c/2} \\ &= (-i\delta t) \cdot \hat{U}_n^{\text{ST}} \left( \hat{H}_n^{c''} - i\delta t (\hat{H}_n^{c'})^2 \right) \hat{U}_{n-1}^{\text{ST}}. \end{aligned} \quad (\text{A29})$$

The exact Hessian elements  $n \geq m$  for this Trotterization scheme are therefore

$$\begin{aligned} \frac{\partial^2 J_F^{\text{ST}_1}}{\partial u_n \partial u_m} &= -\Re \left( \langle \psi_m | \hat{H}_m^{c'} | \chi_m \rangle \cdot \langle \chi_n | \hat{H}_n^{c'} | \psi_n \rangle \right) \delta t^2 \\ &+ \Re \left( o^* \langle \chi_n | \hat{H}_n^{c'} \left( \prod_{j=m+1}^n \hat{U}_j \right) \hat{H}_m^{c'} | \psi_m \rangle \right) \delta t^2 \cdot (1 - \delta_{n,m}) \\ &+ \Re \left( i o^* \langle \chi_n | \left( \hat{H}_n^{c''} - i\delta t (\hat{H}_n^{c'})^2 \right) | \psi_n \rangle \right) \delta t \cdot \delta_{n,m}, \end{aligned} \quad (\text{A30})$$

Derivatives of the end points (corresponding to the outer 'rim' of the Hessian matrix) carry an additional factor 1/2 each, for a total of 1/4 in the corners and 1/2 on the edges. As with the gradient, the Hessian is similarly identical to (A21) when retaining only the  $k = k_{\text{max}} = 0$  term. As an implementation detail, note that the propagated states and operator-state products from (12) may be re-used here. The second term is the most costly to evaluate because of additional state propagations. The order of evaluation should be row-by-row to further increase re-usability of computations.

#### b. Derivatives of $\hat{U}_n^{\text{ST}_2}$

The Suzuki-Trotter expansion reads  $\hat{U}_n^{\text{ST}_2} = \hat{U}_n^{c/2} \hat{U}_n^d \hat{U}_n^{c/2}$ ,

$$\frac{\partial J_F^{\text{ST}_2}}{\partial u_n} = -\Re \left( o^* \frac{\partial o}{\partial u_n} \right), \quad (\text{A31a})$$

$$\frac{\partial o}{\partial u_n} = \left\langle \chi_{n+1} \left| \frac{\partial \hat{U}_n^{\text{ST}_2}}{\partial u_n} \right| \psi_n \right\rangle. \quad (\text{A31b})$$

Invoking Eq. (A14) for  $\hat{U}_n^{c/2}$  we find

$$\begin{aligned} \frac{\partial \hat{U}_n^{\text{ST}_2}}{\partial u_n} &= \frac{\partial \hat{U}_n^{c/2}}{\partial u_n} \hat{U}_n^d \hat{U}_n^{c/2} + \hat{U}_n^{c/2} \hat{U}_n^d \frac{\partial \hat{U}_n^{c/2}}{\partial u_n} \\ &= -\frac{i\delta t}{2} (\hat{U}_n^{c/2} \hat{H}_n^{c'} \hat{U}_n^d \hat{U}_n^{c/2} + \hat{U}_n^{c/2} \hat{U}_n^d \hat{U}_n^{c/2} \hat{H}_n^{c'}) \\ &= -\frac{i\delta t}{2} (\hat{H}_n^{c'} \hat{U}_n^{\text{ST}_2} + \hat{U}_n^{\text{ST}_2} \hat{H}_n^{c'}) \end{aligned}$$

Here we also used that two diagonal matrices always commute, first to evaluate the recursive commutator  $[\hat{H}_n^c, \hat{H}_n^{c'}]_k = \hat{H}_n^c \cdot \delta_{0,k}$  from (A14), and second to recombine the initial propagators since  $[H_n^{c'}, \hat{U}_n^{c/2}] = 0$ . Substituting back into Eqs. A31a-A31b we find

$$\begin{aligned} \frac{\partial o}{\partial u_n} &= -\frac{i\delta t}{2} \left\langle \chi_{n+1} \left| \left( \hat{H}_n^{c'} \hat{U}_n^{\text{ST}_2} + \hat{U}_n^{\text{ST}_2} \hat{H}_n^{c'} \right) \right| \psi_n \right\rangle \\ &= -\frac{i\delta t}{2} \left\{ \left\langle \chi_{n+1} \left| \hat{H}_n^{c'} \right| \psi_{n+1} \right\rangle + \left\langle \chi_n \left| \hat{H}_n^{c'} \right| \psi_n \right\rangle \right\} \\ &= -\frac{i\delta t}{2} \sum_{p=n}^{n+1} \left\langle \chi_p \left| \hat{H}_n^{c'} \right| \psi_p \right\rangle \end{aligned} \quad (\text{A32})$$

$$\Rightarrow \frac{\partial J_F^{\text{ST}_2}}{\partial u_n} = \Re \left( \frac{i o^*}{2} \sum_{p=n}^{n+1} \left\langle \chi_p \left| \hat{H}_n^{c'} \right| \psi_p \right\rangle \right) \delta t, \quad (\text{A33})$$

for all  $n = 1, \dots, N_t - 1$ .

The Hessian elements are written as

$$\frac{\partial^2 J_F}{\partial u_n \partial u_m} = -\Re \left( \left( \frac{\partial o}{\partial u_m} \right)^* \frac{\partial o}{\partial u_n} + o^* \frac{\partial^2 o}{\partial u_n \partial u_m} \right). \quad (\text{A34})$$

and after some lines of calculation, the second derivatives of  $o$  evaluate to

$$\begin{aligned} n > m : \\ \frac{\partial^2 o}{\partial u_n \partial u_m} &= \\ &- \frac{\delta t^2}{4} \sum_{p=n}^{n+1} \sum_{q=m}^{m+1} \left\langle \chi_p \left| \hat{H}_n^{c'} \left( \prod_{j=q}^{p-1} \hat{U}_n^{\text{ST}_2} \right) \hat{H}_m^{c'} \right| \psi_q \right\rangle, \end{aligned} \quad (\text{A35a})$$

$n = m :$

$$\begin{aligned} \frac{\partial^2 o}{\partial u_n \partial u_m} &= -\frac{i\delta t}{2} \left( \sum_{j=n}^{n+1} \left\langle \chi_j \left| \left( \hat{H}_n^{c''} - \frac{i\delta t}{2} (\hat{H}_n^{c'})^2 \right) \right| \psi_j \right\rangle \right. \\ &\quad \left. - i\delta t \left\langle \chi_{n+1} \left| \hat{H}_n^{c'} \hat{U}_n^{\text{ST}_2} \hat{H}_n^{c'} \right| \psi_n \right\rangle \right), \end{aligned} \quad (\text{A35b})$$

Substituting Eqs. A32,A35a,A35b into Eq. (A34) yields the final result,

$$\begin{aligned} \frac{\partial^2 J_F^{\text{ST}_2}}{\partial u_n \partial u_m} &= \Re \left\{ \right. \\ &+ \frac{1}{4} \sum_{p=n}^{n+1} \sum_{q=m}^{m+1} \left\langle \psi_q \left| \hat{H}_m^{c'} \right| \chi_q \right\rangle \left\langle \chi_p \left| \hat{H}_n^{c'} \right| \psi_p \right\rangle \delta t^2 \\ &+ \frac{o^*}{4} \sum_{p=n}^{n+1} \sum_{q=m}^{m+1} \left\langle \chi_p \left| \hat{H}_n^{c'} \prod_{j=q}^{p-1} \hat{U}_n^{\text{ST}_2} \hat{H}_m^{c'} \right| \psi_q \right\rangle (1 - \delta_{n,m}) \delta t^2 \\ &+ \frac{i o^*}{2} \left( \sum_{j=n}^{n+1} \left\langle \chi_j \left| \left( \hat{H}_n^{c''} - \frac{i\delta t}{2} (\hat{H}_n^{c'})^2 \right) \right| \psi_j \right\rangle \right. \\ &\quad \left. - i\delta t \left\langle \chi_{n+1} \left| \hat{H}_n^{c'} \hat{U}_n^{\text{ST}_2} \hat{H}_n^{c'} \right| \psi_n \right\rangle \right) \delta_{n,m} \delta t \left. \right\}. \end{aligned} \quad (\text{A36})$$

Comparatively, the Hessian expression for  $\hat{U}_n^{\text{ST}_2}$  is are much more cumbersome than that for  $\hat{U}_n^{\text{ST}_1}$ .

### 3. Derivatives for Regularizations

For the reasons stated in Sec. III A, it is advantageous to regularize both the control amplitude and its temporal derivative. This requires additional terms in the cost functional objective, imposing discretization, and calculating the respective derivatives. These obviously do not depend on the choice of propagator.

The amplitude regularization is straightforward,

$$J_\alpha = \frac{\alpha}{2} \int_0^T u(t)^2 dt \rightarrow \frac{\alpha}{2} \delta t \sum_{i=1}^{N_t} u_i^2 \quad (\text{A37})$$

$$\frac{\partial J_\alpha}{\partial u_n} = \alpha \delta t u_n, \quad \frac{\partial^2 J_\alpha}{\partial u_m \partial u_n} = \alpha \delta t \delta_{n,m} \quad (\text{A38})$$

where  $\alpha$  is a weighting factor. The derivative regularization is a bit more involved because of end points

$$\begin{aligned} J_\gamma &= \frac{\gamma}{2} \int_0^T \dot{u}(t)^2 dt \rightarrow \frac{\gamma}{8\delta t} \left( \sum_{i=2}^{N_t-1} (u_{i+1} - u_{i-1})^2 \right. \\ &\quad \left. [-3u_1 + 4u_2 - u_3]^2 + [3u_{N_t} - 4u_{N_t-1} + u_{N_t-2}]^2 \right) \end{aligned} \quad (\text{A39})$$

where we used forward (backward) difference approximations for the first (last) point and center approximations for the bulk, all to order  $\mathcal{O}(\delta t^2)$ . The derivative with respect to the first and last three indices is different from the bulk. The resulting gradient written in vector form is

$$\nabla J_\gamma = \frac{\gamma}{4\delta t} \begin{bmatrix} 10u_1 - 12u_2 + 2u_3 \\ -12u_1 + 17u_2 - 4u_3 - u_4 \\ 2u_1 - 4u_2 + 3u_3 - u_5 \\ \vdots \\ 2u_n - u_{n-2} + u_{n+2} \\ \vdots \\ 2u_{N_t} - 4u_{N_t-1} + 3u_{N_t-2} - u_{N_t-4} \\ -12u_{N_t} + 17u_{N_t-1} - 4u_{N_t-2} - u_{N_t-3} \\ 10u_{N_t} - 12u_{N_t-1} + 2u_{N_t-2} \end{bmatrix}, \quad (\text{A40})$$

where the vertical dots extend over the bulk points. Similarly the three first and last Hessian rows are different from the bulk. In a stacking notation where the indices denote the rows:

$$\nabla^2 J_\gamma = \begin{bmatrix} [\nabla^2 J_\gamma]_{1:3} \\ [\nabla^2 J_\gamma]_{4:N_t-3} \\ [\nabla^2 J_\gamma]_{N_t-2:N_t} \end{bmatrix} \quad (\text{A41})$$



where the matrices evaluate to

$$[\nabla^2 J_\gamma]_{1:3} = \frac{\gamma}{4\delta t} \begin{bmatrix} 10 & -12 & 2 & 0 & 0 & 0 & \dots \\ -12 & 17 & -4 & -1 & 0 & 0 & \dots \\ 2 & -4 & 3 & 0 & -1 & 0 & \dots \end{bmatrix}, \quad (\text{A42})$$

$$[\nabla^2 J_\gamma]_{4:N_t-3} = \frac{\gamma}{4\delta t} \begin{bmatrix} 0 & -1 & 0 & 2 & 0 & -1 & 0 & 0 & \dots \\ & & \ddots & & \ddots & & \ddots & & \\ \dots & 0 & 0 & -1 & 0 & 2 & 0 & -1 & 0 \end{bmatrix}, \quad (\text{A43})$$

$$[\nabla^2 J_\gamma]_{N_t-2:N_t} = \frac{\gamma}{4\delta t} \begin{bmatrix} \dots & 0 & -1 & 0 & 3 & -4 & 2 \\ \dots & 0 & 0 & -1 & -4 & 17 & -12 \\ \dots & 0 & 0 & 0 & 2 & -12 & 10 \end{bmatrix}, \quad (\text{A44})$$

where the dots denote continuation of the number they point to.

## Appendix B: Derivation of Bose-Hubbard Model in an Optical Lattice

To obtain Eq. (16) for an optical lattice, one needs to specify the relationship between the lattice parameters and the energetic quantities  $J_x$  and  $U$ . Such relationship is established in the following by solving for the Bloch band structure. We assume a simple cubic periodic lattice approximated near the trap center by

$$V(\vec{r}) \approx \sum_{q=x,y,z} v_q \sin^2 k_l q = V_x + V_y + V_z, \quad (\text{B1})$$

with  $V_q \equiv v_q \sin^2 k_l q$  being the potential in  $q$ -direction with depth  $v_q$ .  $k_l = 2\pi/\lambda_l = \pi/a$  is the laser wavenumber,  $\lambda_l$  is the laser wavelength,  $a$  is the lattice site separation. Thus, the potential is separable in all directions and we may decompose arbitrary wave functions as  $\psi(\vec{r}) = \psi_x \psi_y \psi_z$ . In particular, we may focus on a single direction for the single-particle stationary states. Choosing the  $x$ -direction, we write  $\hat{H}_x^{1p} \phi_k^n(x) = E_k^n \phi_k^n(x)$  where  $n$  is the band index and  $k_l \leq k \leq k_l$  defines the first Brillouin zone of quasi-momentum with intra-equidistant spacing  $\Delta k = 2\pi/L = 2\pi/(N_p \cdot a)$  where  $L$  is the length of the chain. The Bloch wave expansion reads  $\phi_k^n(x) = e^{ikx} u_k^n(x)$  where  $u$  inherits the  $V$  periodicity. The Fourier series for both quantities contains only

a few terms and substitution into the eigenproblem yields a particularly small, simple system of equations for the Fourier expansion coefficients [89] of  $u$ . After numerically obtaining  $\phi_k^n(x)$  for some value of  $v_x$ , we define from the  $n$ 'th band Wannier state centered on site  $i$  by

$$w_{n,x}(x - x_i) = \frac{1}{\sqrt{\mathcal{N}}} \sum_k^{\text{1st Brillouin}} e^{-ikx_i} \phi_k^n(x), \quad (\text{B2})$$

where  $x_i = i \cdot a$  and  $\mathcal{N}$  is a normalization constant. To progress, we make the standard assumptions that the lattice has been loaded in the “trench” of sites defined by  $\vec{r}_i = (x_i, 0, 0)$  and that  $v_y, v_z$  are sufficiently deep to suppress all tunneling events in their respective directions, and that tunneling along  $x$  is nearest neighbor only. Additionally assuming that only the  $n = 0$  band is occupied in each direction ( $2E_R \lesssim v_i$ ) and dropping the index, the bosonic field operator can be expanded as  $\hat{\Psi}(\vec{r}) \approx \sum_{i=1}^{N_p} \hat{a}_{x_i,0,0} \cdot w_x(x - x_i) w_y(y) w_z(z)$ . Inserting this expansion in the many-body Hamiltonian for a dilute bosonic system [90] with  $g_{3D}$  being the two-body interaction strength, one obtains Eq. (16) by letting  $\hat{a}_i \equiv \hat{a}_{x_i,0,0}$  and defining the constitutive relations stated in Eqs. B3-B4. Emphasis has been placed on the implicitly induced dependence on the lattice strengths through the Wannier states. Note the integrals over  $y$  and  $z$  in  $J_x$  is unit due to their normalization, and  $U$  consists of three independent integrals. We consider a realization of the model in a cubic optical lattice loaded with ultra cold atoms. For a cubic optical lattice loaded with ultra cold atoms, the energies are implicitly related to the trapping depths  $v_x, v_y, v_z$  through the Wannier states by the relations

$$J_x(v_x) = - \int_{-\infty}^{\infty} w_x(x - x_i) \hat{H}_x^{1p} w_x(x - x_{i+1}) dx, \quad (\text{B3})$$

$$U(v_x, v_y, v_z) = g_{3D} \int |w_x(x - x_i) w_y(y) w_z(z)|^4 d\vec{r}, \quad (\text{B4})$$

where  $\hat{H}_x^{1p}$  is the single-particle operator in the  $x$ -direction, and  $g_{3D} = 4\pi\hbar^2 a_s/m$  is the two-body collision coupling strength. Note that both  $J_x$  and  $U$  non-trivially depend on  $v_x$ , and although we consider only 1D  $x$ -direction dynamics, the frozen out transverse  $y$ - and  $z$ -directions still implicitly enter in  $U$  by the associated Wannier functions  $w_y$  and  $w_z$ .

- 
- [1] J. P. Dowling and G. J. Milburn, Philosophical Transactions of the Royal Society of London. Series A: Mathematical, Physical and Engineering Sciences **361**, 1655 (2003).
  - [2] A. M. Steane, Fortschritte der Physik: Progress of Physics **46**, 443 (1998).

- [3] E. Knill, Nature **434**, 39 (2005).
- [4] A. G. Fowler, M. Mariantoni, J. M. Martinis, and A. N. Cleland, Physical Review A **86**, 032324 (2012).
- [5] R. Blume-Kohout, J. K. Gamble, E. Nielsen, K. Rudinger, J. Mizrahi, K. Fortier, and P. Maunz, Nature communications **8**, 1 (2017).

- [6] A. Polkovnikov, *Annals of Physics* **326**, 486 (2011).
- [7] T. Feldmann and R. Kosloff, *Physical Review E* **68**, 016101 (2003).
- [8] T. Caneva, A. Silva, R. Fazio, S. Lloyd, T. Calarco, and S. Montangero, *Physical Review A* **89**, 042322 (2014).
- [9] N. Margolus and L. B. Levitin, *Physica D: Nonlinear Phenomena* **120**, 188 (1998).
- [10] V. Giovannetti, S. Lloyd, and L. Maccone, *Physical Review A* **67**, 052109 (2003).
- [11] T. Caneva, M. Murphy, T. Calarco, R. Fazio, S. Montangero, V. Giovannetti, and G. E. Santoro, *Physical review letters* **103**, 240501 (2009).
- [12] S. J. Glaser, U. Boscain, T. Calarco, C. P. Koch, W. Köckenberger, R. Kosloff, I. Kuprov, B. Luy, S. Schirmer, T. Schulte-Herbrüggen, *et al.*, *The European Physical Journal D* **69**, 279 (2015).
- [13] F. Motzoi, J. M. Gambetta, P. Rebentrost, and F. K. Wilhelm, *Physical review letters* **103**, 110501 (2009).
- [14] D. J. Egger and F. K. Wilhelm, *Superconductor Science and Technology* **27**, 014001 (2013).
- [15] M. H. Goerz, F. Motzoi, K. B. Whaley, and C. P. Koch, *npj Quantum Information* **3**, 1 (2017).
- [16] S. Montangero, *Introduction to Tensor Network Methods: Numerical simulations of low-dimensional many-body quantum systems* (Springer International Publishing, 2018).
- [17] M. Dalgaard, F. Motzoi, J. J. Sørensen, and J. Sherson, *npj Quantum Information* **6**, 6 (2020).
- [18] C. T. Kehlet, A. C. Sivertsen, M. Bjerring, T. O. Reiss, N. Khaneja, S. J. Glaser, and N. C. Nielsen, *Journal of the American Chemical Society* **126**, 10202 (2004).
- [19] N. Khaneja, T. Reiss, C. Kehlet, T. Schulte-Herbrüggen, and S. J. Glaser, *Journal of magnetic resonance* **172**, 296 (2005).
- [20] N. C. Nielsen, C. Kehlet, S. J. Glaser, and N. Khaneja, *eMagRes* (2007).
- [21] W. Kallies and S. J. Glaser, *Journal of Magnetic Resonance* **286**, 115 (2018).
- [22] J. J. Sørensen, J. S. Nyemann, F. Motzoi, J. Sherson, and T. Vosegaard, *The Journal of Chemical Physics* **152**, 054104 (2020).
- [23] J. Scheuer, X. Kong, R. S. Said, J. Chen, A. Kurz, L. Marseglia, J. Du, P. R. Hemmer, S. Montangero, T. Calarco, *et al.*, *New Journal of Physics* **16**, 093022 (2014).
- [24] F. Dolde, V. Bergholm, Y. Wang, I. Jakobi, B. Naydenov, S. Pezzagna, J. Meijer, F. Jelezko, P. Neumann, T. Schulte-Herbrüggen, *et al.*, *Nature communications* **5**, 1 (2014).
- [25] G. Waldherr, Y. Wang, S. Zaiser, M. Jamali, T. Schulte-Herbrüggen, H. Abe, T. Ohshima, J. Isoya, J. Du, P. Neumann, *et al.*, *Nature* **506**, 204 (2014).
- [26] Y. Chou, S.-Y. Huang, and H.-S. Goan, *Physical Review A* **91**, 052315 (2015).
- [27] C. P. Koch, J. P. Palao, R. Kosloff, and F. Masnou-Seeuws, *Physical Review A* **70**, 013402 (2004).
- [28] C. P. Koch, E. Luc-Koenig, and F. Masnou-Seeuws, *Physical Review A* **73**, 033408 (2006).
- [29] E. F. De Lima, T.-S. Ho, and H. Rabitz, *Chemical Physics Letters* **501**, 267 (2011).
- [30] K. M. Tibbetts, X. Xing, and H. Rabitz, *Physical Chemistry Chemical Physics* **15**, 18012 (2013).
- [31] P. Doria, T. Calarco, and S. Montangero, *Physical review letters* **106**, 190501 (2011).
- [32] S. van Frank, M. Bonneau, J. Schmiedmayer, S. Hild, C. Gross, M. Cheneau, I. Bloch, T. Pichler, A. Negretti, T. Calarco, and S. Montangero, *Scientific Reports* **6**, 34187 (2016).
- [33] M. Mundt and D. J. Tannor, *New Journal of Physics* **11**, 105038 (2009).
- [34] G. Jäger and U. Hohenester, *Physical Review A* **88**, 035601 (2013).
- [35] J. Cui, R. van Bijnen, T. Pohl, S. Montangero, and T. Calarco, *Quantum Science and Technology* **2**, 035006 (2017).
- [36] S. Patsch, D. M. Reich, J.-M. Raimond, M. Brune, S. Gleyzes, and C. P. Koch, *Physical Review A* **97**, 053418 (2018).
- [37] P. De Fouquieres, S. Schirmer, S. Glaser, and I. Kuprov, *Journal of Magnetic Resonance* **212**, 412 (2011).
- [38] S. Machnes, U. Sander, S. Glaser, P. de Fouquieres, A. Gruslys, S. Schirmer, and T. Schulte-Herbrüggen, *Physical Review A* **84**, 022305 (2011).
- [39] S. Machnes, D. J. Tannor, F. K. Wilhelm, and E. Assémat, *arXiv:1507.04261* (2015).
- [40] J. Sørensen, M. Aranburu, T. Heinzel, and J. Sherson, *Physical Review A* **98**, 022119 (2018).
- [41] D. J. Tannor, V. Kazakov, and V. Orlov, in *Time-dependent quantum molecular dynamics* (Springer, 1992) pp. 347–360.
- [42] J. P. Palao and R. Kosloff, *Physical review letters* **89**, 188301 (2002).
- [43] S. G. Schirmer and P. de Fouquieres, *New Journal of Physics* **13**, 073029 (2011).
- [44] T. Caneva, T. Calarco, and S. Montangero, *Physical Review A* **84**, 022326 (2011).
- [45] D. Sels, *Physical Review A* **97**, 040302 (2018).
- [46] X. Li, D. Pecak, T. Sowiński, J. Sherson, and A. E. Nielsen, *Physical Review A* **97**, 033602 (2018).
- [47] J. J. Sørensen, M. Aranburu, T. Heinzel, and J. Sherson, *arXiv:1802.07521* (2018).
- [48] D. Dong and I. R. Petersen, *IET Control Theory & Applications* **4**, 2651 (2010).
- [49] F. Caruso, S. Montangero, T. Calarco, S. F. Huelga, and M. B. Plenio, *Physical Review A* **85**, 042331 (2012).
- [50] I. Walmsley and H. Rabitz, *Physics Today* **56**, 43 (2003).
- [51] S. Rosi, A. Bernard, N. Fabbri, L. Fallani, C. Fort, M. Inguscio, T. Calarco, and S. Montangero, *Physical Review A* **88**, 021601 (2013).
- [52] G. Feng, F. H. Cho, H. Katiyar, J. Li, D. Lu, J. Baugh, and R. Laflamme, *Physical Review A* **98**, 052341 (2018).
- [53] R. Heck, O. Vuculescu, J. J. Sørensen, J. Zoller, M. G. Andreassen, M. G. Bason, P. Ejlersen, O. Elfasson, P. Haikka, J. S. Laustsen, L. L. Nielsen, A. Mao, R. Müller, M. Napolitano, M. K. Pedersen, A. R. Thorsen, C. Bergenholtz, T. Calarco, S. Montangero, and J. F. Sherson, *Proceedings of the National Academy of Sciences* **115**, E11231 (2018), <https://www.pnas.org/content/115/48/E11231.full.pdf>.
- [54] J. H. M. Jensen, M. Gajdacz, S. Z. Ahmed, J. H. Czarkowski, C. Weidner, J. Rafner, J. J. Sørensen, K. Mølmer, and J. F. Sherson, *arXiv:2004.03296* (2020).
- [55] J. Nocedal and S. J. Wright, *Numerical optimization 2nd* (Springer Science & Business Media, New York, 2006).
- [56] D. Poulin, A. Qarry, R. Somma, and F. Verstraete, *Physical review letters* **106**, 170501 (2011).
- [57] G. Vidal, *Physical review letters* **91**, 147902 (2003).

- [58] S. Lloyd and S. Montangero, Physical review letters **113**, 010502 (2014).
- [59] D. Pérez-García, F. Verstraete, M. M. Wolf, and J. I. Cirac, *Quantum Information & Computation* **7**, 401 (2007).
- [60] G. Vidal, Physical review letters **93**, 040502 (2004).
- [61] J. V. Porto, S. Rolston, B. Laburthe Tolra, C. J. Williams, and W. D. Phillips, Philosophical Transactions of the Royal Society of London. Series A: Mathematical, Physical and Engineering Sciences **361**, 1417 (2003).
- [62] S. Hild, T. Fukuhara, P. Schauß, J. Zeiher, M. Knap, E. Demler, I. Bloch, and C. Gross, Physical review letters **113**, 147205 (2014).
- [63] T. Caneva, T. Calarco, R. Fazio, G. E. Santoro, and S. Montangero, Physical Review A **84**, 012312 (2011).
- [64] D. Quiñones-Valles, S. Dolgov, and D. Savostyanov, “Tensor product approach to quantum control,” in *Integral Methods in Science and Engineering: Analytic Treatment and Numerical Approximations*, edited by C. Constanda and P. Harris (Springer International Publishing, Cham, 2019) pp. 367–379.
- [65] “Chapter 5: Discretization schemes,” in *Formulation and Numerical Solution of Quantum Control Problems* (Society for Industrial and Applied Mathematics, 2017) pp. 181–220.
- [66] U. Schollwöck, Annals of Physics **326**, 96 (2011).
- [67] G. C. Hegerfeldt, Physical review letters **111**, 260501 (2013).
- [68] G. E. Santoro, R. Martoňák, E. Tosatti, and R. Car, Science **295**, 2427 (2002).
- [69] M. Greiner, O. Mandel, T. Esslinger, T. W. Hänsch, and I. Bloch, nature **415**, 39 (2002).
- [70] M. Lewenstein, A. Sanpera, V. Ahufinger, B. Damski, A. Sen, and U. Sen, Advances in Physics **56**, 243 (2007).
- [71] I. M. Georgescu, S. Ashhab, and F. Nori, Reviews of Modern Physics **86**, 153 (2014).
- [72] T. D. Kühner and H. Monien, Physical Review B **58**, R14741 (1998).
- [73] T. D. Kühner, S. R. White, and H. Monien, Physical Review B **61**, 12474 (2000).
- [74] W. H. Zurek, U. Dorner, and P. Zoller, Physical review letters **95**, 105701 (2005).
- [75] J. Zhang and R. Dong, European Journal of Physics **31**, 591 (2010).
- [76] L. Kohn, P. Silvi, M. Gerster, M. Keck, R. Fazio, G. E. Santoro, and S. Montangero, Physical Review A **101**, 023617 (2020).
- [77] S. Ejima, H. Fehske, F. Gebhard, K. zu Münster, M. Knap, E. Arrigoni, and W. von der Linden, Physical Review A **85**, 053644 (2012).
- [78] A. J. Daley, C. Kollath, U. Schollwöck, and G. Vidal, Journal of Statistical Mechanics: Theory and Experiment **2004**, P04005 (2004).
- [79] S. Paeckel, T. Köhler, A. Swoboda, S. R. Manmana, U. Schollwöck, and C. Hubig, Annals of Physics **411**, 167998 (2019).
- [80] ITensor Library (version 2) <http://itensor.org>.
- [81] A. Wächter and L. T. Biegler, Mathematical programming **106**, 25 (2006).
- [82] J. Dziarmaga and W. H. Zurek, Scientific reports **4**, 5950 (2014).
- [83] A. G. Day, M. Bukov, P. Weinberg, P. Mehta, and D. Sels, Physical review letters **122**, 020601 (2019).
- [84] More bang for the buck, as it were.
- [85] J. Sørensen, J. H. M. Jensen, T. Heinzl, and J. Sherson, Computer Physics Communications **243**, 135 (2019).
- [86] J. H. M. Jensen, J. J. Sørensen, K. Mølmer, and J. F. Sherson, Physical Review A **100**, 052314 (2019).
- [87] M. L. Boas, *Mathematical methods in the physical sciences* (John Wiley & Sons, 2006).
- [88] J. J. Sakurai and E. D. Commins, “Modern quantum mechanics, revised edition,” (1995).
- [89] M. Weidemüller and C. Zimmermann, *Interactions in ultracold gases: from atoms to molecules* (John Wiley & Sons, 2011).
- [90] F. Dalfovo, S. Giorgini, L. P. Pitaevskii, and S. Stringari, Reviews of Modern Physics **71**, 463 (1999).